NASA Contractor Report 189155
QUEST Technical Report 534

P- 59

A New Unsteady Mixing Model to Predict NO_x Production During Rapid Mixing in a Dual-Stage Combustor

Suresh Menon
QUEST Integrated, Inc.
Kent, Washington

April 1992

Prepared for
Lewis Research Center
Under Contract NAS3–26242

NASA
National Aeronautics and Space Administration

TABLE OF CONTENTS

1. INTRODUCTION

To develop the next generation of high-speed civil transport (HSCT) aircraft, a significant reduction in pollutant emissions from the engine must first be demonstrated. Emissions that must be reduced include NOx emissions into the stratosphere during supersonic flight and the NOx, CO, and unburned hydrocarbons emissions near urban areas during idling and takeoff/landing operations. One candidate low-NOx combustor is a dual-stage combustor consisting of a fuel-rich primary stage, a quick quench zone, and a secondary fuel-lean burn stage. Significant NOx production appears to occur primarily in the quick quench zone during the unsteady mixing process. Numerical steady-state prediction models are incapable of including the effects of unsteady mixing. This Phase I work demonstrates a novel unsteady mixing model that, when used in current numerical prediction codes to account for the mixing process, will provide the necessary correction, resulting in an improved analysis tool of great use to the engine designer.

Extensive investigations have been carried out by various researchers (e.g., McVey and Kennedy, 1979; Westmoreland et al., 1979; Bahr, 1980; Mularz, 1979; Cooper, 1979; Semerjian et al., 1979; Tang and Churchill, 1981; Tacina, 1990) to identify and evaluate various advanced combustor designs that could result in reduced pollutant emissions. It is well-known that NOx production is kinetically controlled (an exponential function of adiabatic combustor temperature) and occurs due to the availability of free oxygen atoms in hot regions. Therefore, a low-NOx combustor design must minimize or eliminate free oxygen atoms in the hot regions without decreasing the combustion efficiency of the combustor and without increasing the emission of CO and unburned hydrocarbons. Various low-NOx combustor concepts—i.e., Lean-Premixed-Prevaporized (LPP), Rich Burn/Quick Quench/Lean Burn (RQL), and Direct Injection (DI)—are being studied and their NOx emission characteristics have been determined over a wide range of inlet temperatures, fuel-air ratios, and pressures (Tacina, 1990). Current data indicate that the LPP concept, which involves premixing fuel vapor with air and burning at low temperature, has the lowest NOx emission. However, this concept has a major operational disadvantage due to its narrow stability limits. The DI concept, which involves direct injection of the fuel into the combustor, has shown promise in that it has increased stability limits and also produces low NOx emissions comparable to that produced by the LPP combustor. However, results for the DI concept so far have been obtained with gaseous fuels, and it is not clear whether the same characteristics will be observed with liquid fuels (Tacina, 1990).

For aircraft such as the HSCT, which will have a wide range of operating conditions, the RQL combustor configuration has good potential for significantly reducing NOx emissions. An idealized RQL configuration is shown in Figure 1. In such a configuration, the primary combustion occurs in a fuel-rich environment. Downstream, air is injected to rapidly dilute the fuel-rich mixture exiting from the primary zone so that a uniformly mixed fuel-lean mixture burns in the secondary combustion zone. This concept, although more complex than the LPP and the DI concepts, attempts to minimize (if not completely inhibit) NOx formation in the hot primary stage by limiting or eliminating free oxygen atoms and in the fuel-lean secondary stage by reducing the combustion temperature. NOx will form in regions where the secondary air mixes with the hot fuel-rich mixture exiting from the primary zone (in the quench region), especially in regions where the fuel-air ratio becomes locally close to stoichiometric. In fact, current data appear to indicate that most of the NOx may be forming in the mixing region. However, the exact mechanism of NOx production in the highly unsteady mixing zone has not yet been clarified. The RQL concept has good stability characteristics due to its fuel-rich zone and can be used with current jet fuels as well as alternative fuels containing large amounts of fuel-bound nitrogen (Tacina, 1990). Thus, if an effective technique to rapidly mix the secondary air

with the fuel-rich mixture can be determined, this concept may become practically feasible.

At present, there is an extensive experimental program underway to evaluate low-NOx combustors such as the LPP and the RQL (Ott, 1990). Detailed measurements inside and immediately downstream of the quench zone will be required to determine the efficiency of the rapid mixing concepts. Experimentally studying various types of rapid mixing concepts such as swirl jets and jets in crossflow can be expensive, and unless the characteristic length and time scales involved in these unsteady mixing concepts are determined and their relevance to NOx production quantified, the experiments alone may not provide the necessary guidelines to build production engines. Typically, numerical prediction methods are used to complement experimental studies, both to understand the dynamics and to extend the experimental results to unmeasured or unmeasurable operating conditions. However, most numerical schemes currently used for prediction purposes are based on steady-state schemes (e.g., Correa, 1984; Correa and Shyy, 1987; Magnussen and Hjertager, 1977; Swithenbank et al., 1980; Nguyen and Bittker, 1989) and are unable to account for the highly unsteady phenomena occurring during rapid mixing. Some earlier attempts to include the effects of unsteady mixing (e.g., Pope and Correa, 1986; Pratt, 1980; Butler and Pratt, 1986; Chen and Dibble, 1990) have resulted in somewhat improved predictions. In principle, simulation techniques such as large-eddy simulations (LES) could be used to understand and predict more accurately the unsteady mixing processes, but they are impractical for engineering design analysis due to the substantial computational resources required. Therefore, there is a critical need to develop a more accurate yet simple model for unsteady mixing processes that can be used in conjunction with conventional steady-state methods so that the computed results are corrected for the unsteady processes occurring in the mixing region. The development and demonstration of such an unsteady mixing model are described in this report.

A numerical approach that models unsteady flow fields must reflect two practical objectives: (1) the physics of the flow field must be modeled as *accurately* as possible to ensure reliable predictions, and (2) the numerical technique must provide the design engineer with information as *fast* as possible to improve and optimize the design. In reality, these two objectives are often in conflict, and thus a compromise is necessary.

The mixing between the fuel-rich mixture and the secondary air is an unsteady process occurring in a highly turbulent environment where significant fluctuations in both the velocity and temperature field will occur. Velocity fluctuations will affect the turbulent transport and mixing of the various species, and the temperature fluctuations will affect the chemical kinetics rates leading to non-equilibrium production/destruction of species. In fact, the prediction of thermal NO production based on the assumption that the O atoms are in equilibrium with O_2 (Peters and Donnerhack, 1981) has been shown to be in error due to significant non-equilibrium concentration of O and other radicals in turbulent nonpremixed flames (Drake et al., 1987).

Another physical consequence of secondary air injection into the fuel-rich mixture is that in regions where these two streams come into contact, a shear layer will form. Such shear layer regions are well-known to be susceptible to instability and will roll up into vortices. These vortices then undergo pairing and merging processes, resulting in large coherent vortices that subsequently break down into small-scale turbulence. Such structures are known to play a major role in entrainment and mixing processes, and their effect on mixing needs to be taken into account. For example, there could be regions where the local fuel-air ratio is near stoichiometry, and this could result in large NOx production if the temperature is high. Rapid mixing concepts typically attempt to break down these structures as quickly as possible so that turbulent mixing will be enhanced. However, there may still

be regions in the mixing zone where these vortices persist for some time, and so the characteristic length (or size) and time scales associated with their formation and breakdown need to be included in the unsteady mixing model.

Studies of molecular mixing have shown that the mixing process generally consists of two steps: (1) the entrainment of the fluid from the two streams into the mixing region, and (2) the mixing of the fluids at the molecular level as they come into contact. Classical modeling of turbulent mixing in high Reynolds number flows typically assumes that turbulent convection dominates over molecular diffusion processes, i.e., the first step is the crucial one. However, recent studies at CalTech (for a summary, see Dimotakis, 1989) have revealed that, for flows at the same Reynolds number, both the mixing rates and the distribution of the mixed fluids were quite different in fluids of widely different molecular diffusivity. This clearly demonstrated that, besides turbulent convection, molecular diffusion effects are also important at the small scales. In terms of nondimensional parameters, this implies that the effects of both the Reynolds number and the Schmidt number on the mixing rate need to be taken into account. When chemical reactions are also occurring, the Damkohler number effect will also need to be included.

Kerstein (1988, 1989, 1990, 1991a, 1991b) took into account these earlier results and developed a novel model called the *linear-eddy* model, which treats *separately* the effects of both *turbulent convection* and *molecular mixing* at the small scales. It was demonstrated that this model is capable of accurately describing many features of turbulent mixing and chemical reactions in turbulent shear layers, nonpremixed flames, and turbulent jets. This successful demonstration of the linear-eddy model has laid the basic groundwork to further develop the mixing model for application to practical problems such as the prediction of NO production in the quench zone of the RQL combustor. In this Phase I study, a configuration-invariant mixing model has been developed so that it is applicable to a wide variety of flows. Furthermore, this mixing algorithm has been developed so that it can be implemented within the framework of well-used prediction codes to account for the unsteady mixing effects. This coupling issue will be addressed in Phase II.

2. PHASE I TECHNICAL OBJECTIVES

The overall Phase I technical objective was to demonstrate the potential of the linear-eddy unsteady mixing model to take into account the characteristic mixing lengths and time scales within a mixing zone. To demonstrate its capability, this model was used to study a mixing situation similar to that which would occur in the quench zone of an RQL combustor.

The specific technical objectives of the Phase I study were:

- To formulate the linear-eddy model to characterize the unsteady mixing between the fuel-rich primary mixture and the secondary air stream;
- To implement a reaction mechanism within the linear-eddy mixing model; and
- To demonstrate the ability of the linear-eddy model to predict NO production in the mixing zone.

As described in this report, all the above technical objectives were successfully achieved. The results of this research will be presented in the near future (Menon et al., 1992).

3. FORMULATION OF THE MIXING MODEL

The basic model and its application to a wide range of turbulent flows with and without chemical reactions has been described by Kerstein in a series of papers (Kerstein, 1988, 1989, 1990, 1991a, 1991b). The motivation for these studies was to develop a configuration-invariant approach to study turbulent flows. Kerstein's results showed that a set of laws or models governing the processes of entrainment, turbulent mixing, and thermochemistry can be developed to provide a self-contained picture of the overall fluid mechanical and thermochemical structure of turbulent reacting flows. His studies further showed that the same model is capable of predicting, for example, the observed differences between shear layer mixing and thermal mixing layer in grid turbulence (Kerstein, 1988, 1989). In this Phase I study, this model has been extended to study unsteady mixing and thermochemical processes similar to those occurring in a mixing zone. Multispecies mixing, propane-air nonpremixed flame and hydrogen-air nonpremixed flame problems were computed to demonstrate the capabilities of the mixing model developed in this research.

3.1 The Linear-Eddy Unsteady Mixing Model

The basic idea of the original formulation is to treat separately the two different mechanisms acting to describe the evolution of a scalar(s) (chemical species) in a specified domain. These two mechanisms are *molecular diffusion* and *turbulent convective transport*. For flows in which finite-rate kinetics is occurring, some additional mechanisms need to be incorporated, as will be discussed in the Section 3.2.

3.1.1 Molecular Diffusion

The first mechanism is *molecular diffusion*, which is implemented by the numerical time integration of the diffusion equation

$$\frac{\partial Y_k}{\partial t} = W_k + D_k \frac{\partial^2 Y_k}{\partial x_i^2} \tag{1}$$

where Y_k is the kth species mass fraction, W_k is the chemical production/destruction term for the kth species, and D_k is the kth species diffusion coefficient. In principle, this diffusion equation could be solved in the full three-dimensional form. However, the strategy here is to resolve *all* the relevant length scales involved in the local diffusion and transport processes. Note that it is in the *small scales* where mixing and chemical reactions occur; thus, resolution of the small scales is important. Conventional time-accurate simulation techniques (e.g., direct numerical simulations) attempt to resolve all the small scales numerically, resulting in prohibitive computational cost. Also, the resolution possible using current supercomputers only allows simulations of flows at low Reynolds numbers, which are not indicative of realistic systems. Even when subgrid models are used in LES techniques to increase the Reynolds number, the computational cost is still quite high.

Therefore, to keep the computational cost reasonable and to resolve all the small scales taking part in the unsteady mixing, the domain is restricted to one dimension; hence the term *linear-eddy*. Kerstein (1988, 1989, 1990, 1991a) applied this model to various types of turbulent shear flows and obtained good agreement with experimental data. Note that although Equation (1) is solved in one dimension, the information on the volume of the cells is built into the algorithm implicitly. This aspect will be described later.

For the purpose of discussion, consider a reaction mechanism between two species, A and B, such that

$$A + B \rightarrow P \tag{2}$$

More complex reaction mechanisms typical of propane-air and hydrogen-air nonpremixed flame combustion have been studied in Phase I, as discussed later. The reaction rate for the mechanism in Equation (2) is

$$W = k_1[A][B] \tag{3}$$

Thus, for this reaction mechanism, the Fickian diffusion equation (1) becomes in one dimension

$$\frac{\partial Y_a}{\partial t} - D_{ab}\frac{\partial^2 Y_a}{\partial x^2} = \frac{\partial Y_b}{\partial t} - D_{ab}\frac{\partial^2 Y_b}{\partial x^2} = -kY_aY_b \tag{4}$$

where k is the normalized rate constant.

The application of the linear-eddy model to a particular flow configuration depends both on the configuration and on the issues that need to be addressed. In the earlier formulations (Kerstein, 1988, 1989) the linear-eddy dimension (the computational domain) was chosen as a transverse (y-direction) line co-moving with the mean streamwise flow, and the streamwise development of the mixing region (x-direction) was obtained by relating it to the temporal evolution in the diffusion equation by the relation $x = Ut$, where U is the convective velocity. In a more recent study of turbulent nonpremixed flames (Kerstein, 1991a), it was shown that the choice of the *streamwise* direction as the linear-eddy computational domain is more advantageous, especially for the study of the axial structure of the flow based on the fluxes of mass, momentum, etc., through transverse planes.

Consider the configuration shown in Figure 2, which shows a fuel jet exiting into a mixing zone. This is a test geometry that corresponds to the mixing zone in the RQL combustor and other geometries similar to diffusion mixing and combustion in many experiments. Thus, demonstration of the mixing model in this geometry should provide the necessary validation for this Phase I study.

If the x-direction is chosen as the linear-eddy domain, and if that domain is further subdivided into small cells, then each cell would represent a control volume, which is determined by the cell width (Δx), and a radial zone extending from the centerline to the nominal jet radius (r_j). The volume of each cell of width Δx is then given by $V(x) = \pi r_j^2 \Delta x$. For the case shown in Figure 2, the jet radius is given by the relation

$$r_j(x) = C_\epsilon(x - x_0) \tag{5}$$

where x_0 is the virtual origin and C_ϵ is an empirical constant which ranges from 0.07 in the forced-convection limit to 0.10 in the natural-convection limit. The choice of Δx is dependent on the smallest characteristic length scale (or eddy size) that needs to be resolved. Kerstein (1991a) chose $\Delta x = L(x)/n$, where $L(x)$ is the integral length scale, which is given by $L(x) \approx 2r_j(x)$, and n is the resolution factor, which is constant for a given computed realization. Typically, $n = 50$ was chosen for this study based on the analysis by Kerstein who found that this resolution is sufficient for many

of the earlier studies of turbulent mixing. The importance of the resolution will be addressed in more detail in the next phase. Using the definition of $L(x)$ given above, the volume of each cell becomes $V(x) = \frac{\pi}{4} L(x)^2 \Delta x$.

Since we are interested in the downstream evolution of the mixing region, the spatial evolution of the jet needs to be incorporated. From experimental data, the spreading of the jet can be given as

$$\frac{L(x)}{d_\theta} = 1 + cx \tag{6}$$

where d_θ is the momentum diameter of the jet, which is defined as $d_\theta = d_0\sqrt{\rho_0/\rho_a}$ and c is a constant denoting the spatial spreading rate; typically, $c = 0.14$ for free jet. Here, $x = x^*/d_\theta$, where x^* is the dimensional streamwise distance. Also, ρ_0 and ρ_a are respectively, the density of the primary fuel stream at the inlet (i.e., at $x = 0$) and the ambient (air) density. Note that, with this definition of $L(x)$, the cell width Δx and the volume $V(x)$ increases in the downstream distance. The increase in the volume reflects the entrainment of air into the mixing region. For the RQL combustor, the free jet spreading rate may not be applicable since mixing will be occuring in a confined region. Therefore, simulations with different values of the spreading rate parameter, c were performed to address the effect of modifying the effect of air entrainment. Some of these results are described in this report.

In addition to the specification of the spreading rate of the mixing layer, it is also necessary to decide the total streamwise extent of the mixing layer that must be simulated. Typically, this distance is specified as the distance at which self-similarity is achieved. Experiments suggests that a region $x/d_0 \approx 200$ needs to be simulated since the premixed flame length typically can be in the range of $x/d_0 = 100-140$. In all the present calculations, the spatial extent of the mixing layer was divided into 25 blocks, and each block was then divided into 50 cells. Thus, the total number of cells used for the computation was 1250. Note that, since the integral length scale increases with downstream distance, the size of the blocks increases in the streamwise direction. With the resolution used in this study, and with the spreading rate given by equation (6) (with $c = 0.14$), the total length of the mixing layer exceeds $x/d_0 = 200$. This was sufficient for most of the nonpremixed flame combustion problems studied here. The effect of increasing the resolution and the streamwise extent of the mixing region have not yet been investigated, since this would increase the computational cost of each simulation. However, the calculations discussed in this report clearly demonstrate the capability of the numerical scheme, and the resolution used is considered sufficient for the Phase I validation study.

Once the cell size (Δx), the spreading rate, the total number of cells, and the initial conditions (to be discussed later) are specified, the diffusion mechanism [Equation (1)] can be solved in a purely deterministic fashion using standard finite-difference schemes.

3.1.2 Turbulent Convection

The second mechanism in the linear-eddy model is the *turbulent convection* process. This is incorporated in the model by a random process that rearranges the fluid element along the linear direction and is carried out (subject to some constraints) while the diffusion process is going on. This process causes a random walk of the fluid elements and introduces a discontinuous (turbulent) fluid motion, representing small-scale convective stirring. Each event involves permutation of the cells of the spatially discretized concentration field and is confined to a finite segment of the total computational

domain. This finite domain may be viewed as the size of the eddy that is causing the turbulent stirring. To bring the physics of turbulent transport into this process, the frequency of these events corresponding to a given range of eddy sizes is determined such that the principal scaling laws governing turbulent transport are satisfied.

To implement this process of turbulent transport, two different rearrangement processes have been developed by Kerstein (1989, 1991a). These are the *block inversion* and the *triplet map*. The effect of both these processes are graphically described in Figure 3. The triplet map (Figure 3b) is used in all the calculations discussed in this report, and is described below.

Figure 3b shows the effect of the *triplet map* in the continuum limit. Essentially, the size of the eddy (as described below) is first chosen from a probability distribution of eddy sizes. For this discussion, let us choose an eddy size of length l. Then the scalar field within the chosen segment l is compressed by a factor of three, thus tripling the scalar gradient within the segment. The original scalar field within the segment l is then replaced by three copies of this compressed field, with the middle copy reversed. The resulting scalar field is shown in Figure 3b. This discrete mapping is defined so as to recover this rule in the continuum limit while satisfying species conservation exactly in the discrete implementation. Since in the present case the cell volumes are increasing in the downstream direction, some care is required to take into account the unequal volumes of the cells.

To describe the actual implementation of the triplet map, let us assume that the segment chosen of length l is in the discrete formulation made up of 12 cells. Let l consist of cells that are numbered 1,2,3,4,5,6,7,8,9,10,11,12. When the triplet map is used to compress and rearrange the cells, the resulting new sequence will be 1,4,7,10,11,8,5,2,3,6,9,12. The cells themselves are not physically moved; rather, the species in the cells are exchanged in this manner.

The triplet map can be understood on both an intuitive and a theoretical basis. Intuitively, consider the effect of a single clockwise eddy on the scalar field that initially has a uniform gradient in the field. This is shown in Figure 4a. The effect of the eddy will be to distort the scalar gradient in the field, which would then take a form similar to that shown in Figure 4b. Comparing this figure with the effect of the triplet map (Figure 3b), it can be seen that the mapping procedure essentially reflects this phenomenon. More details of the theoretical considerations behind the triplet map are given in Kerstein (1990c).

As noted earlier, to carry out the triplet map, the size of the eddy l must be first determined. The sizes of eddies present in the flow was assumed to range from the Kolmogorov microscale η to the integral length scale L (i.e., $\eta < l < L$) and the eddy size l was chosen randomly from a power-law distribution $f(l)$ within this chosen range.

Once the range of eddy sizes is known, a single inversion event involves first choosing a eddy size l from the pdf $f(l)$ (which needs to be determined) and carrying out the spatial inversion described above. Note that $f(l)$ varies with both x and t. A sequence of such inversions must be carried out so that all allowable block sizes (or eddies) within the chosen range take part in the process. The rate at which this inversion takes place is determined based on the local values and therefore varies both with time and with the spatial location in the mixing region. This inversion rate is specified by a rate parameter λ, which has the unit of (length x time)$^{-1}$. This inversion rate is determined by first determining the turbulent diffusivity of the random walk process for each eddy. The turbulent diffusivity of a random marker is then the sum of the contributions due to all the eddies taking part in the inversion events. Without going into detail (see Kerstein, 1989), the total diffusivity associated with the

random walk of all eddies up to a size l_o (where $\eta < l_0 < L$) is

$$D_t(l) = \int_{\eta}^{l_0} \frac{\lambda}{6} l^3 f(l) dl \tag{7}$$

Using Kolmogorov scaling, $\mathrm{Re}_{l_0} \approx (l_0/\eta)^{3/4}$, Kerstein derived an expression for $f(l)$, which can be written as

$$f(l) = \frac{5}{3L} \frac{1}{(L/\eta)^{5/3} - 1} \left[\frac{l}{L}\right]^{-5/3} \tag{8}$$

Using this expression in Equation (7), the value of λ can be determined by setting $l_0 = L$ and $D_t = \nu \mathrm{Re}_L$. This is given as (Kerstein, 1989)

$$\lambda = \frac{54}{5} \frac{\nu \mathrm{Re}_L}{L^3} \frac{[(L/\eta)^{5/3} - 1]}{1 - (\eta/L)^{4/3}} \tag{9}$$

For high Reynolds number flows, $L \gg \eta$, the leading-order approximation to Equation (9) is

$$\lambda = \frac{54}{5} \frac{\nu \mathrm{Re}_L}{L^3} \left[\frac{L}{\eta}\right]^{5/3} \tag{10}$$

In the algorithm, the full expression [Equation (9)] is used. The time scale associated with the random stirring events, τ_s, is related to the rate parameter λ by the simple relation $\tau_s = 1/\lambda L$.

This completes the description of the basic model. To summarize, the unsteady mixing in a specified domain is modeled by two processes that work together but which are modeled separately. Molecular diffusion updates the concentration fields deterministically based on Fickian diffusion within a linear domain in which all the relevant small scales are resolved. The typical time scale for this diffusion process is related to the cell spacing, Δx, and the diffusion coefficient D as $\tau_d = \Delta x^2/D$. Chemical heat release within each cell in the linear domain can also be included in this diffusion process by solving the diffusion equations for k species with the full chemistry model for W_k. However, the finite-rate kinetics of interest in this study is a multispecies mechanism (described in the next section) with large production/destruction terms for W_k (and thus, small chemical times, τ_{ch}). This can make the diffusion equation numerically stiff. Therefore, we will implement the finite-rate kinetics in a different way within the linear-eddy, as described in the next section.

While the molecular diffusion process is going on, it is punctuated by randomly occurring rearrangement events, representing the turbulent convective stirring process. Thus, stirring occurs at a frequency λ, as determined by the physical scaling laws described above, and results in the rearrangement of the species within each eddy of size l. Typically, the time (frequency) at which the inversion events take place will be different than the time-step required for integrating the diffusion equation. In most cases, $\tau_s \ll \tau_d$, and thus a series of inversion events have to be carried out with a characteristic time (τ_s) between each diffusion step. For example, if $\tau_d \approx n\tau_s$, then n inversion steps have to be carried out before the next diffusion step can take place. This is taken into account in the algorithm.

3.2 Application-Specific Processes

The basic processes, molecular diffusion and turbulent mixing must be further supplemented by application-specific processes that characterize the type of unsteady mixing being studied. By parametrically varying the important parameters of the application-specific process, the effect of different unsteady mixing strategies can be studied. In Phase II, these application-specific processes will be handled differently since the mixing algorithm will be incorporated with steady-state prediction codes. However, the physics involved in the application-specific processes will not be much different. Some of the issues are described briefly below.

Figure 2 shows a characteristic case in which a fuel jet and an air jet enter a mixing zone. A variant of this type of mixing process is the more complex shear flow due to jets in crossflow. Such complex mixing scenarios will be considered in the next phase. For the configuration shown in Figure 2, there are three application-specific processes that need to be modeled. They are fuel inflow, air entrainment, and streamwise motion of the mixture. Each of these processes is described below.

3.2.1 Fuel Inflow

For the linear-eddy application, the streamwise direction is divided into cells of width Δx and volume $V(x)$, as described above. Fuel enters the first cell of volume $V(0)$ at a constant mass flow rate $\dot{m}_0$ from the upstream state. The state conditions—e.g., the temperature, pressure, density, and the species mass fractions in the fuel mixture at the entrance to the mixing zone—need to be specified. In all the calculations described here, this state is specified. For the RQL combustor, this state may be the exit conditions from the primary zone.

3.2.2 Air Entrainment

The process of air entrainment is a major facet of this model. The entrainment process is determined based on the length and time scales associated with the corresponding physical process. Thus, by proper modification of the entrainment law, the effect of different air injection strategies could be studied. Although this issue will be addressed in more detail in the next phase, some preliminary study of modifying the entrainment process was carried out in Phase I, and is described later.

From previous experimental observations, it is clear that the air will be entrained throughout the flow domain; however, it is not entrained in a continuous manner. Rather, it appears that the air is entrained in finite parcels, and that and the size of the parcel directly influences the mixing process. From earlier experiments (e.g., Dahm and Dimotakis, 1987; Mungal and Hollingsworth, 1989; Mungal and O'Neil, 1989) it appears that the size of the parcel is comparable to the jet diameter. This information is included in the model by setting the volume of the entrained air parcel to be $V_E(x) = (\pi/4)L^3(x)$. Note that, since $L(x)$ is an increasing function with x, the volume of air entrained will also increase with streamwise distance.

Thus, the entrainment of air parcels of volume $V_E(x)$ will occur throughout the domain. The frequency of the entrainment events in the interval $(x, x + dx)$ is given by $\lambda_E(x)dx$, and is determined from the local entrainment rate from the relation

$$\frac{d\dot{m}_a}{dx} = \lambda_E(x)\rho_\infty V_E(x) \tag{11}$$

where $\dot{m}_a$ is the mass flux of the air crossing any x plane. Based on the exit conditions at the fuel jet, the mass flux from the fuel jet $\dot{m}_f(0, t) = \dot{m}_{f0}(t)$ will be known. To obtain the mass flux of the entrained air at any x plane, $\dot{m}_a(x)$, the use of entrainment laws is necessary. For example, the simplest law is given by Ricou and Spalding (1961) which was modified by Becker and Yamazaki (1978) to obtain

$$\frac{d\dot{m}_a}{dx} = C_E \left[\frac{\pi\rho\dot{G}}{4}\right]^{1/2} \tag{12}$$

where $\rho = \dot{m}/\dot{V}$, and $\dot{V}$ and $\dot{G}$ are, respectively, the volume and momentum flux crossing any x plane. For this generalized law, C_E is an empirical coefficient that ranges from 0.32 in the forced-convection limit to 1.84 in the natural-convection limit.

The momentum flux $\dot{G}(x)$ is determined from the local momentum balance according to the relation

$$\frac{d\dot{G}}{dx} = \pi C_g g(\rho_\infty - \rho) b^2 \tag{13}$$

where g is the gravitational acceleration, $C_g = 11.8$ is an empirical coefficient, and b is the nominal jet radius defined earlier in Equation (5).

For specific modeling of different mixing concepts, the entrainment laws need to be determined either empirically or from theoretical/experimental studies. In all the studies described in this report, Equation (13) is integrated with the inflow condition, $\dot{G}(0) = G_0$, where, $G_0 = (\pi/4)\rho_0 u_0^2 d_0^2$ where, subscript 0 denotes the incoming state of the primary fuel stream at the inlet. This result is used in Equation (11) to obtain the entrainment rate $\lambda_E(x)$.

The entrainment events occurring at the frequency λ_E are taken to be statistically independent (similar to the inversion events), and the implementation process is chosen to be similar to the turbulent stirring process described earlier. Thus, the epochs and locations of the entrainment events are selected by an algorithm that parallels the stirring algorithm described earlier.

Note that when the entrainment events are taken to be statistically independent, the effect of coherent vortical motion cannot be included in the model. For accurate prediction of combustion in shear flows, the effect of coherent motion must be included since it is known to exist in shear flows and its effects on mixing and entrainment processes are well-documented. As noted before, however, organized entrainment patterns are configuration-specific; thus, to include their effect on the overall entrainment process would require specific input depending on the type of shear flow being studied. The exact modifications to the entrainment law necessary to include the effect of coherent vortical motions in the mixing layer will be considered in more detail in the next phase.

3.2.3 Streamwise Motion

When fuel enters the first cell, it must displace fluid in subsequent cells to maintain constancy of the cell volume. This displacement induces a streamwise flow. In some respects, this reactant-feed mechanism resembles earlier plug-flow studies (e.g., the coalescence-dispersion model of Pratt, 1980). However, there are two major differences. First, the radial spreading of the jet is included in the present model by virtue of the streamwise increase of the cell volumes (see Figure 2). Second,

although the fuel will enter at only one location (the exit from the primary combustor), the air will be entrained throughout the streamwise direction, as shown in Figure 2. Both these realistic mechanisms are included in the present model, whereas they are missing in the plug-flow mixing models.

3.3 Implementation of Reaction Mechanism Within the Linear-Eddy Model

As noted in the above section, conceptually, there is no problem to include the finite-rate kinetics within each cell of the linear-eddy during the molecular diffusion process. However, the small time scales associated with the finite-rate kinetics will make the time-step very small and increase the overall computational cost. To reduce the computational cost, a more practical approach is used. Figure 5 shows how the finite-rate kinetics algorithm fits into the linear-eddy algorithm.

In this study, *three* different mixing and reaction mechanisms were implemented to demonstrate the capability of the mixing model developed in this research. Here, we will describe each of the approaches.

3.3.1 Multispecies Mixing

For a series of calculations, the effect of multispecies mixing processes in the jet was studied. For this demonstration, the primary stream or the fuel jet was chosen to consist of five species. Most of the calculations were performed using species O_2, N_2, O, N, and NO with specified mass fractions at the inlet ($x = 0$) and with a specified inlet temperature. Some simulations were also carried out for a mixture that mimiced the distribution exiting from the RQL combustor. The air stream was assumed to contain only two species, O_2 and N_2, again with specified mass fractions and temperature. The mixing and diffusion process between the species from the fuel jet and the entrained air stream was then computed for various fuel temperatures, fuel jet velocities, and initial species distributions. The diffusion process was modeled by solving Equation (1) for Y_k where k = 1,5. In some simulations, the effect of modifying the entrainment process was also studied. No reaction was assumed to occur for most of the mixing studies ($W_k = 0$). However, since the initial distribution contained both O atoms and N_2, it was possible to estimate the formation of NO using a global NO production mechanism given by Chen and Kollman (1991). This mechanism can be used to estimate the formation of NO (in gm/cm^3 - s) by

$$W_{NO} = 2k_f[N_2][O]M_{NO} \tag{14}$$

where M_i is the ith species molecular weight, [C] denotes the concentration of species C (moles/cm^3), and $k_f = 1.84x10^{14}\exp(-38370/T)$ cm^3/mole - s. It must be pointed out that this NO production rate was determined by Chen and Kollmann (1991) for the H_2-air combustion mechanism (described below) and is used here only to demonstrate the effect of mixing on the NO production mechanism. The effect of finite-rate kinetics and the associated NO production was studied in more detail using the H_2-air combustion mechanism as discussed below.

3.3.2 Propane-Air Nonpremixed Flame

For this study, the earlier study by Kerstein (1991b) was repeated using the new code. To study this type of flame, a reduced mechanism can be used in terms of the mixture fraction ξ, which at any x location is given by

$$\xi(x) = \frac{\dot{m}(0)}{\dot{m}(x)} \tag{15}$$

where $\dot{m}(0)$ is the mass flux at the entrance (the fuel jet). Thus, the inflow condition (at $x = 0$) for this case is given by $\xi = 1$.

The thermochemistry of the propane-air flame is treated by assuming equilibrium chemistry and adopting the Shvab-Zeldovich assumptions so that the local density depends only on the local mixture fraction, $\rho = \rho(\xi)$. Thus, the axial variation of the density can then be determined once $\xi(x)$ is determined. The relation between ρ and ξ for propane-air combustion based on equilibrium chemistry (Gordon and McBride, 1971) is determined in the range $0 < \xi < 0.15$. For larger values of ξ, soot begins to form and thus invalidates the equilibrium assumption. The functional form is

$$\frac{\rho(\xi)}{\rho_\infty} = \left[\left\{1+\left[\frac{\rho_\infty}{\rho_o}-1\right]\xi\right\}\left\{1+\left[\frac{T_f}{T_\infty}-1\right]\min\left[\frac{\xi}{\xi_{st}},\frac{1-\xi}{1-\xi_{st}}\right]\right\}\right]^{-1} \tag{16}$$

where ξ_{st} denotes the stoichiometric value (for the propane-air nonpremixed flame, $\xi_{st} = 0.0601$), and T_f is the adiabatic flame temperature (here, $T_f = 2283\ K$). This expression is valid for $\xi < 0.15$; for $0.15 < \xi < 1.0$, the density is obtained by extrapolation.

To determine $\xi(x)$, the diffusion equation (1) is solved with Y_k replaced by ξ. Thus, the diffusion equation becomes

$$\frac{\partial \xi}{\partial t} = D_\xi \frac{\partial^2 \xi}{\partial x^2} \tag{17}$$

The molecular transport coefficient D_ξ in Equation (17) and the molecular viscosity ν are updated in each cell at each time based on a $T^{1.7}$ dependence, i.e., $D(T) = CT^{1.7}$ and $\nu = ScD$, where, Sc is the Schmidt number which is a specified input (typically, $Sc = 0.406$). To obtain the temperature variation, we used the equilibrium relation for density to get

$$\frac{T(\xi)}{T_\infty} = 1+\left[\frac{T_a}{T_\infty}-1\right]\min\left[\frac{\xi}{\xi_{st}},\frac{1-\xi}{1-\xi_{st}}\right] \tag{18}$$

Finally, an estimate of NO production in the propane-air flame by the thermal mechanism (the so-called Zelodovich mechanism) can be estimated. Here, we use the approximate expression of Peters and Donnerhack (1981) for the thermal NO production rate S_{NO} per unit mass. This relation is

$$S_{NO} = BM_{NO}\frac{Y_{N_2}}{M_{N_2}}\left[\frac{\rho Y_{O_2}}{M_{O_2}}\right]^{1/2}\exp(-Q/T) \tag{19}$$

where B = $5.74x10^{14}$ $(cm^3/mole)^{1/2}/sec$ and Q = 66,900. This expression was obtained by assuming that O atoms are in chemical equilibrium with O_2 molecules.

This expression has been criticized by Drake et al. (1987) because significant superequilibrium concentrations of O and other radicals occur in turbulent nonpremixed flames. They estimated that the prediction by Equation (19) is off by a factor of 2.5.

To determine the NO production rate S_{NO} for the propane flame, the terms in Equation (19) are rewritten in terms of ξ. To obtain the mass production of NO, the NO rate in each cell is summed over all linear-eddy cells and divided by $\dot{m}(0)$ to obtain the emission index.

3.3.3 Hydrogen-Air Nonpremixed Flame

For the propane-air nonpremixed flame problem described above, the diffusion process was reduced to the solution of a single equation for the mixture fraction ξ and all other properties could then be determined by using equilibrium assumptions. For more realistic combustion problems with finite-rate kinetics, detailed reaction mechanisms need to be incorporated. However, it is well-known that using full finite-rate kinetic mechanism can cause significant numerical stiffness (due to large production/destruction terms) and can significantly increase the computational cost. An approach that reduces the computational effort is to use *reduced mechanisms* that result in the reduction of the number of equations that must be solved. Numerical computations using reduced mechanisms have been employed for engineering analysis (e.g, Correa and Shyy, 1987; Chen and Kollman, 1990) and is an acceptable approach. Since our intention is to couple this mixing model to conventional prediction methods for engineering analysis, the demonstration of a reduced mechanism within theis mixing model is very important. This has been carried out for the case of a hydrogen-air nonpremixed flame problem.

The hydrogen-air flame problem has been in the past both experimentally (e.g., Magre and Dibble, 1988) and numerically (e.g., Chen and Kollmann, 1990). Also, a reduced mechanism model has been developed by Chen. This model has been used in the framework of the pdf method to predict the flow properties (e.g., Chen and Kollmann, 1990). The primary advantage of the reduced mechanism approach is the reduction in the number of scalars that need to be solved. For example, for the hydrogen-air problem, only two scalars—the mixture fraction ξ and a progress variable n—need to be solved to obtain all other properties, as described below. Also, the reaction mechanism can be solved first to generate a *look-up* table that can then be used to interpolate for the species information whenever required. This clearly reduces the amount of computation required. This reduction of computational effort is important in the present case since the present model accurately computes the mixing aspect, and if the look-up table procedure can be coupled with the mixing model, then the overall computational cost will not be significantly more than that for the case of mixing alone. This has indeed been accomplished in this study.

In the hydrogen-air nonpremixed flame problem considered here, the following ten elementary reactions are considered:

Reaction	A_i	b_i	E_i	
$H + O_2 = OH + O$	1.2×10^{17}	−0.91	69.1	(R1)
$O + H_2 = OH + H$	1.5×10^{7}	2.0	31.6	(R2)
$OH + H_2 = H_2O + H$	1.0×10^{8}	1.6	13.8	(R3)
$OH + OH = H_2O + O$	3.4×10^{13}	0.0	21.0	(R4)
$H + HO_2 = OH + OH$	1.5×10^{14}	0.0	4.2	(R5)
$H + OH + M = H_2O + M$	2.15×10^{22}	−2.0	0.0	(R6)
$H + H + M = H_2 + M$	1.83×10^{18}	−1.0	0.0	(R7)
$O + O + M = O_2 + M$	2.86×10^{18}	−1.0	0.0	(R8)
$H + O + M = OH + O$	6.2×10^{16}	−0.6	0.0	(R9)
$H + O_2 + M = HO_2 + M$	2.0×10^{18}	−0.8	0.0	(R10)

Here, the rate constants for the ith reaction are given by

$$k_i = A_i T^{b_i} \exp\left[-\frac{E_i}{RT_i}\right] \tag{20}$$

and the coefficients A_i, b_i, and E_i are obtained from Warnatz (1984) with units of cm, mol, KJ, and K. The third-body collision efficiencies, z_i, relative to H_2 are also taken from Warnatz (1984) as $z_{H_2} = 1$, $z_{O_2} = 0.4$, $z_{N_2} = 0.4$, $z_{H_2O} = 6.5$, and $z_{Ar} = 0.35$. The total number of scalars in this reaction mechanism is ten, which are the seven active chemical species (i.e., H_2, O_2, H_2O, O, H, OH, HO_2) plus temperature, pressure, and density. If we assume equal diffusivities for species and enthalpy, the mixing process can be described by a conserved scalar ξ. The mixture fraction is defined as the normalized mass fraction of an atomic species originating in the fuel stream. With this definition, the concentrations of atomic species are linearly related to ξ. For example, for the H_2-air system, three conservation equations for H and O atoms can be derived as

$$n_H + n_{OH} + 2n_{H_2} + 2n_{H_2O} + n_{HO_2} = 2\frac{\xi Y_{H_2}}{M_{H_2}} \tag{21}$$

$$n_O + n_{OH} + 2n_{O_2} + n_{H_2O} + 2n_{HO_2} = 2\frac{\phi(1-\xi)}{M_{N_2} + \phi M_{O_2}} \tag{22}$$

$$h = \xi h_1 + (1 - \xi)h_2 \tag{23}$$

where n_i and M_i are the number of moles per unit mass and the molecular weight of the ith species, respectively, and ϕ is the ratio between the O and N atom concentrations in air. Thus, $\phi = 0.21/0.79$, and Y_i is the mass fraction of the ith species in the fuel.

The partial equilibrium model was used by Janicka and Kollmann (1982) and assumes that the reactions R1-R5 are relatively fast compared to the three-body recombination steps R6-R10. Thus, the partial equilibrium model for R1-R5 provides four independent relations of the form

$$K_1 n_H n_{O_2} = K_{-1} n_{OH} n_O \tag{24a}$$

$$K_2 n_O n_{H_2} = K_{-2} n_{OH} n_H \tag{24b}$$

$$K_3 n_{OH} n_{H_2} = K_{-3} n_{H_2} n_H \tag{24c}$$

$$K_4 n_H n_{HO_2} = K_{-4} n_{OH} n_{OH} \tag{24d}$$

which results in the global one-step reduced reaction mechanism

$$2H_2 + O_2 = 2H_2O \tag{25}$$

The reaction rate for the global reaction can be written in terms of the rates for the elementary steps:

$$r_i = r_6 + r_7 + r_8 + r_9 + r_{10} \tag{26}$$

where r_i denotes the forward reaction rate for the ith elementary step with units of moles/(mass-time). With these relations, in addition to the mixture fraction ξ, only one more reactive scalar is required to describe the combustion process. In this study, following the work by Chen and Kollmann (1991), the total number of moles per unit mass, n, is chosen as the reactive scalar. By definition,

$$n = n_{H_2} + n_{O_2} + n_{H_2O} + n_O + n_{OH} + n_H + n_{HO_2} + n_{N_2} \tag{27}$$

The allowable domain for n at a given ξ needs to be determined. The allowable maximum occurs when fuel and air are mixed without reaction. Then the maximum n is

$$n_{\max} = \frac{\xi Y_{H_2}}{M_{H_2}} + \frac{(1-\xi)(1+\phi)}{M_{N_2} + \phi M_{O_2}} \tag{28}$$

and the allowable minimum occurs when hydrogen and oxygen combine to form water without forming any radical. Two possible states can occur depending upon the value of the mixture fraction ξ. When $\xi < \xi_{st}$, the minimum value is given as

$$n_{\min} = \frac{\xi Y_{H_2}}{2M_{H_2}} + \frac{(1-\xi)(1+\phi)}{M_{N_2} + \phi M_{O_2}} \tag{29}$$

For $\xi > \xi_{st}$ the minimum value is

$$n_{\min} = \frac{\xi Y_{H_2}}{2M_{H_2}} + \frac{(1-\xi)}{M_{N_2} + \phi M_{O_2}} \tag{30}$$

Two types of hydrogen-air combustion process has been studied in this Phase I. A pure hydrogen-air case with a stoichiometric conditions, $\xi_{st} = 0.028$, $n_{st} = 0.0412$ and a 22% Argon+78% hydrogen -air case with stoichiometric conditions, $\xi_{st} = 0.1632$, $n_{st} = 0.0388$. The latter combustion problem was studied due to the availability of some experimental data (Magre and Dible, 1988) with which comparison could then be made.

A nondimensional reaction progress variable n^* can be also be defined as

$$n^* = \frac{n_{max} - n}{n_{max} - n_{min}} \tag{31}$$

which has two states: $n^* = 0$ when the mixture is completely unburnt, and $n^* = 1$ when the mixture is completely burnt to form water. Then, according to the global reaction, equation (25), the rate equation for n^* at a fixed mixture fraction ξ is

$$(\frac{dn^*}{dt})_\xi = \frac{1}{n_{max} - n_{min}} \left[r_6 + r_7 + r_8 + r_9 + r_{10} \right] \tag{32}$$

Either this equation or an equation for $\frac{dn}{dt}$ can be used for the progress variable. In this study, the equation for $\frac{dn}{dt}$ was used.

The mechanism used to model the formation of NO in the H_2-air combustion process is primarily from the thermal pathways. Thus, for now, the prompt NO formation and the formation of NO involving intermediate N_2O are neglected. This is considered acceptable for now, since in general the majority of NO formed is from the thermal NOx pathways. More complete NO production mechanisms will be considered in the next phase.

The thermal NO reactions are described by the well-known Zeldovich mechanism as

$$N_2 + O = NO + N \tag{NR1}$$

$$O_2 + N = NO + O \tag{NR2}$$

$$N + OH = NO + H \tag{NR3}$$

If a steady-state assumption for the N atom is assumed, and $[NO]/[NO]_{equil} \ll 1$ is assumed, the Zeldovich reaction mechanism can be reduced to a single global step as

$$N_2 + O_2 = 2NO \tag{NR4}$$

with $r_{nr4} = r_{nr1}$, and the NO formation rate (gm/cm^3 - s) can be approximated as

$$S_{NO} \approx 2k_{f,nr1} \left[N_2\right] \left[O\right] M_{NO} \tag{33}$$

where $[C]$ denotes the concentration of species C (moles/cm^3), M_{NO} is the molecular weight of NO, and $k_{f,nr1} = 1.84x10^{14}\exp(-38370/T)$ cm^3/mole - s.

The diffusion problem analogous to equation (1) for this hydrogen-air case is the solution of two equations for the mixture fraction ξ and the progress variable n. They can be written as

$$\frac{\partial \xi}{\partial t} = D_\xi \frac{\partial^2 \xi}{\partial x^2} \tag{34}$$

and

$$\frac{\partial n}{\partial t} = D_n \frac{\partial^2 n}{\partial x^2} + \left[\frac{dn}{dt}\right]_\xi \tag{35}$$

Here, the source term in equation (35) (i.e., dn/dt) can be obtained from the look-up table for the reduced mechanism as described above. Also, for this study, we assumed that $D_\xi = D_n = \nu/Sc$, where ν is determined using the Sutherland's law.

4. IMPLEMENTATION OF THE MIXING AND REACTION ALGORITHMS

The implementation of the linear-eddy model as a numerical algorithm is relatively straightforward. However, since the description given in Section 3 covers various mechanisms that must be coupled together, the steps involved in the actual implementation are described here. Figure 5 illustrates the processes involved in the linear-eddy algorithm.

The first step is to initialize the fuel flow entering the mixing zone (at $x = 0$) by prescribing the velocity, initial temperature, species distribution, Reynolds and Schmidt numbers, and so on. In a full implementation to the RQL combustor (to be carried out in Phase II), this initial flow field information will be exit plane data from the steady-state calculations in the primary fuel-rich combustion zone. However, if this model is used also in the primary stage (this is possible since this mixing model is configuration-invariant), then the inflow conditions can be the conditions at the entrance to the combustor. The algorithm described in Section 3 involves *six* separate mechanisms: the *fuel feed* into the mixing zone, the *air entrainment* process throughout the mixing zone, the *molecular diffusion* process, the *turbulent stirring* and the *finite-rate kinetics* process within each cell, and the *displacement* process resulting from the effects of entrainment and thermal expansion due to combustion (discussed below). The implementation of these mechanisms is outlined below.

First, molecular diffusion is carried out by time integration of the diffusion equation within the mixing region using a standard finite-difference approach. Typically, the time-step τ for the numerical integration is $\tau = C\eta^2/D_{ab}$, where η is the size of the smallest (Kolmogorov) eddy (in the implementation, $\eta = \Delta x_{\min}$) and $C < 1$ for stability.

The other main mechanism, i.e., the triplet map event that models small-scale turbulent stirring, is also carried out. The triplet map does not take place continuously while the numerical integration of Equation (4) (or Equation (17) for the propane-air or Equations (34) and (35) for the hydrogen-air nonpremixed flame cases) is being carried out; rather, it occurs whenever the epoch of the inversion event is reached during the time integration. Typically, the epoch of the mapping event is randomly selected based on the overall rate, $R = \lambda L$, of such events. When this time is reached, the location of the eddy is selected, with uniform likelihood within the cell, and a eddy size is chosen by randomly sampling the pdf $f(l)$. Then the mapping process is carried out as described earlier. This exchange is assumed to occur simultaneously and instantaneously so that no time elapses during this process. After this event, the epoch of the next event is determined based on the new value of the event rate R. In many cases, the time scale for the mapping is much smaller than the diffusion time step and thus, a series of mapping are carried out till such time as the next diffusion step is required.

Similar to the turbulent stirring events, the entrainment of the air parcels into each cell is also determined based on the entrainment law and the entrainment frequency λ_E; also, the epochs and locations of the entrainment events parallel the above-described inversion process. As the fuel and entrained air are being diffused and stirred within each cell of the linear-eddy, chemical kinetics will also be occurring that will further change the chemical composition, temperature and density in each cell.

The fuel feed, air entrainment, and thermal expansion due to combustion all induce streamwise fluid displacement, which represents the streamwise flow. This displacement process is implemented as a distinct computational step that incorporates all three contributions. After the fuel feed, air entrainment, and combustion during a time-step have been completed, the deviation of the cell densities from their equilibrium values is used to determine new equilibrium values using perfect gas law

and a streamwise adjustment of the fluid properties in the cells carried out to adjust the properties in each cell.

This completes the description of the procedure for implementing the linear-eddy algorithm to study unsteady mixing and combustion in a finite domain characteristic of a mixing zone. Note that the above discussion has identified various length and time scales that are involved in the mixing and combustion processes. The relationship between these scales will directly determine the effectiveness of the mixing strategy.

5. RESULTS AND DISCUSSION

In this section, we describe the results of the various tests and simulations carried out to demonstrate the capability of the mixing model that was developed in this Phase I study. Since detailed data for the RQL combustor are not available, we decided to carry out a series of calculations designed to be more general than the mixing configuration representative of the RQL quench zone. This was considered acceptable for the Phase I study since the basic technical objective was to develop a general-purpose mixing model that can be used in conjunction with predictive schemes. The actual implementation of the mixing model in a practical design analysis code will be carried out in Phase II. Direct comparison and parametric studies of the mixing strategy for the problems of specific interest will also be carried out in Phase II.

The results of the Phase I study fall into three different categories in an ascending order of complexity. The first set of calculations was carried out to demonstrate the model's capability to handle multispecies mixing. Typically, the primary fuel entering the mixing zone was assumed to consist of five species with initially specified mass fraction distributions, and the entrained air was assumed to consist of two species (N_2 and O_2). However, the code was written so that an arbitrary number of species could be simulated if required. In some of the mixing studies, the species responsible for NOx formation (see reactions NR1-NR4) were allowed to mix in the mixing zone, and an estimation of the NO production based on a global reaction mechanism was made.

The second set of calculations was carried out for a propane-air buoyant nonpremixed flame, for which a simple model has been demonstrated before (Kerstein, 1991b). In this model, all flow properties are determined by the evaluation of a conserved scalar ξ through the use of equilibrium assumptions. The formation of NOx in this nonpremixed flame problem was also estimated using a global mechanism as described in Section 3.3.2.

Finally, the third set of calculations was closer to the more representative combustion approach used in many calculations for practical applications (e.g., Chen and Kollmann, 1990, 1991). For demonstration, we chose to study the H_2-air combustion system. To reduce the complexity of the finite-rate kinetics and to reduce the computational cost, a reduced-mechanism approach was employed. A look-up table for the H_2-air combustion was created in terms of two scalars: a conserved scalar ξ and a progress variable n; An option was included to generate a look-up table in terms of three scalars (i.e., ξ, n, and h), where h is the enthalpy of the mixture. This option is typically used when the effect of radiation heat loss needs to be incorporated. However, for the Phase I study, it was decided to use only the two-scalar look-up table. This look-up table was incorporated within the framework of the mixing model, and a series of computations was carried out for the H_2-air nonpremixed flame.

Since the computations are carried out for a long time, the spatial distribution will change from instant to instant. As the time increases, the flow eventually reaches a statistically steady state; the instantaneous realizations can be Favre-averaged to obtain the steady picture of the flow field. To obtain the steady-state field, the total number of grid points (1250 in the present case) is divided into blocks each containing 50 cells; each block is then further divided into bins containing 10 cells each. Favre-averaging of the flow variables is then carried out over each bin (10 cells) to obtain the averaged property. In general, the Favre-averaging process results in

$$\tilde{\phi} = \frac{\sum_{1}^{10} \rho V \phi}{\sum_{1}^{10} \rho V} \tag{36}$$

where ϕ denotes any flow property of interest, V is the volume of each cell, and the summation is for each bin containing 10 cells. Most of the results presented in this section are in terms of these Favre-averaged properties, since these are typically the properties required for design and prediction. However, note that since the integral length scale, $L(x)$, and Δx are both increasing in the streamwise direction, the total volume in each block is also increasing in the streamwise direction. Thus, when the Favre-averaged properties are plotted as a function of the *blocks*, in the physical space (i.e., x/d_0) the scale is nonlinear. This is reflected in most of the figures as noted below.

All computations were carried out on an IBM PC compatible (486), since access to a supercomputer was not provided in the Phase I study. The resource and time constraints of the Phase I study limited the number of the simulations that could be carried out.

5.1 Multispecies Mixing and NOx Formation

The first series of test cases involved modeling the effect of mixing between multispecies. For these tests, we assumed that the primary fuel stream consists of five species (O_2, N_2, O, N, and NO) with specified mass fractions (Y_i) and with an initial temperature of 2100 K. The entrained air was modeled by two species (O_2 and N_2) at 300 K. The reference primary fuel jet speed was 12 m/s and the secondary air was initially at stagnant conditions. Tests to study the effects of varying the fuel jet speed, the initial mass fraction distribution, and the entrainment conditions were carried out. Only representative results are shown here. Table I shows the various test cases discussed in this section.

Figure 6 shows a test case (M-1) with turbulent mixing and air entrainment occurring for the full extent of the jet. A spreading parameter of $c = 0.05$ was used in equation (6), which essentially modifies the air entrainment process. Also, since now $L(x)$ does not increase rapidly in the downstream direction, for the resolution used (1250 cells) the streamwise extent for these simulations was limited to $x/d_0 < 50$. Figures 6a through 6d show, respectively, the species mass fractions Y_{N_2}, Y_{NO}, and Y_O and the mixture density ρ/ρ_a. Since this simulation is a pure mixing case, there is no reaction occurring and the flow field shown here is representative of the single realization of the axial distribution of the flow properties. Figure 6a shows that near the exit of the primary fuel jet there is hardly any nitrogen present (due to the initial condition, see Table I), but as the air is entrained, the nitrogen content increases downstream. The axial variation of all the species looks the same since all species diffusion coefficients were assumed to be the same, and the effect of turbulent mixing on all the species was also the same. As the jet spreads due to air entrainment, the density (Figure 6d) increases in the far field, since there the mixture is mostly air.

Figure 7 shows another test case which was similar to case M-1 shown in Figure 6 except that for $x/d_0 < 13$ (or the first ten blocks), no stirring (turbulent mixing) or air entrainment was allowed to occur. Constraints such as this are one way to mimic different mixing strategies. For this condition, the constraints imply that for $x/d_0 < 13$, the mixture from the inlet undergoes simple diffusion without mixing with the secondary air. This is clearly reflected in the instantaneous species, density, and temperature distribution in the jet as shown in Figure 7. Also, in this case, NO production based on the global hydrogen-air jet flame model (Chen and Kollmann, 1991) given earlier was used to estimate the NO production (test case M-3). The results of three cases (M-1 through M-3) are summarized in

Figures 8a through 8c, which show the Favre-averaged flow properties. Note that in these plots the x −axis is in terms of the blocks (1 to 25), which is related to the streamwise distance (x/d_0) non-linearly as shown in Figure 8a. As noted before, as the block location increases downstream, the physical spacing increases due to the increase in the cell size Δx. For case M-3 (with NO production), it can be seen that the peak NO production is close to the location where air was allowed to be entrained ($x/d_0 = 13$, Figure 8b). This is a consequence of suddenly allowing the air to be entrained in a large parcel (since the volume of the block is large), which then mixes with the hot primary stream causing rapid production of NO. Since NO is being produced at the expense of O-atoms, the mass fraction for oxygen atoms decreases rapidly (Figure 8c) for test case M-3. As the O atoms become negligible, the NO production also decreases very rapidly. Note that, for this test case, there are sufficient N_2 molecules available for the NO production mechanism. Thus, for this case, the important species is the O-atom, which was only available from the initial distribution from the fuel jet.

Parametric studies such as this with various entrainment conditions may be able to identify the important mixing strategy that will minimize NO production in the RQL combustor.

Figure 9 shows another test case (M-4) for which the initial species distribution in the fuel jet was adjusted so that the fuel stream entering the mixing zone contains no N_2 molecules and no NO molecules (see Table I). Also, in this case, the free jet spreading rate $c = 0.14$ was used, and mixing and air entrainment were allowed to occur the entire extent of the mixing zone. In these calculations, the streamwise length of the mixing region exceeds $x/d_0 = 200$. Figure 9a shows the spatial distribution of Y_{N_2} for this test case. As the jet spreads, around $x/d_0 = 25$, the entrainment of air (which contains a significant amount of N_2) causes the increase of N_2 content in the mixing region. Mixing with the cold air stream causes the temperature of the fuel jet to decrease very rapidly. A consequence of this effect is that NO production is limited to a small region near the zone where the entrained air is mixing with the fuel stream. This is seen in Figure 9b. Figure 9c shows the Favre-averaged distribution of the N_2, O_2 and NO molecules as a function of the blocks. Again, peak production of NO is observed in the region where the hot fuel stream is mixing with the cold entrained air at around $x/d_0 = 25$.

Finally, for reference, we carried out a simulation using representative conditions as reported in Howe et al., (1991) with the conditions at the exit of the primary stage of the RQL combustor entering the quench zone (see Table I). Figures 10a through 10c show, respectively, an instantaneous realization of the temperature, the oxygen mass fraction Y_{O_2}, and the water mass fraction Y_{H_2O} variation in the streamwise direction for this test case. No combustion was allowed to occur, and this simulation was carried out just to see the extent to which the streamwise penetration of the fuel stream will occur in the absence of reactions.

5.2 Propane-Air Diffusion Flame

A series of test cases was studied similar to the cases studied earlier by Kerstein (1991a). This is a model problem of a buoyant propane-air nonpremixed flame. Both the primary fuel and the secondary air were assumed to be at the same temperature (300 K) and the flame temperature was 2280 K (see Table II). The effect of increasing the fuel jet velocity was studied. Figure 11 shows the typical instantaneous realization of the axial variation of the various flow properties for a specified fuel jet speed (test case P-1). As the fuel enters the mixing region, whereever the mixture fraction becomes stoichiometric, the fuel is converted to product and the temperature rises to the adiabatic flame

temperature. This is reflected in Figures 11a and 11b. Further downstream only air is present, which is at a much higher density.

Figure 12 shows the instantaneous flow properties for another test case (P-4) which was for a much higher jet speed of 72 m/s. In this case the fuel penetrates further downstream in the streamwise direction (Figure 12a), and more regions with high temperature in the mixing region are seen (Figure 12b).

Figure 13a shows the time-averaged density field in the jet for various jet velocities. As the fuel jet speed increases, the increase in density occurs further downstream. This is similar to the results obtained earlier by Kerstein (1991a). Figure 13b shows the effect of carrying out the computations twice as long. Here, t_1 is the time at which the simulation was stopped. Typically, the simulations should be carried out long enough so that the flow properties reach a statistically steady state. Figure 13b shows that, for this simulation, the far field has still not reached a statistically steady state; however, the difference between the two simulations is not very significant. Resource and time constraints of the Phase I study made it difficult to carry out the simulations long enough to reach a statistical steady state everywhere. The intent of this Phase I study was only to demonstrate the potential capability of the mixing model.

Validation of the mixing model was carried out earlier by Kerstein (1991a) where the simulations were performed for the propane-air case in more detail. Since that study is quite relevant for the present work, the important conclusions are briefly noted here by using some of those results. Figure 13c shows the time-averaged density field as a function of streamwise distance (which is nondimensionalized by the jet momentum diameter, d_θ). The linear-eddy model predictions are compared to experimental results of Becker and Yamazaki (1978) and to the predictions of an "instant" mixing model. Clearly, the linear-eddy model is capable of providing improved predictions when compared to the instant mixing model.

Since NOx production was allowed to occur based on the global mechanism as given in equation (19), it was possible to estimate the emission index for NO as a function of time of evolution for the entire mixing region. Figures 14a through 14c show the NO emission index as a function of nondimensional time for various fuel jet speeds (NOTE: the emission index is given here in *kg/kg of fuel* and to determine the standard value in *gm/kg of fuel* the value igiven here must be multiplied by 1000). Here, the time $\bar{t} = t/t_0$, where $t_0 = d_\theta/u_{jet}$. Thus, for increasing jet speeds, t_0 becomes smaller. We must point out that the NO emission estimate shown in Figure 14 was obtained only at a few times (marked by solid circles), and the large fluctuation in time seen in these figures may not be meaningful since the in-between time values were not recorded. Also, the simulations were not carried out long enough to reach a statistically steady state due to resource (computer) and time constraints.

Figures 15a through 15c show the axial variation of the NO production rate for various jet speeds. These plots indicate that as the jet speed increases the peak production of NO moves further downstream. Figure 15c also shows the effect of carrying out the simulation for twice as long. The flow field has clearly reached a statistically steady state at nearly the entire jet except for the region of peak NO production.

5.3 Hydrogen-Air Diffusion Flame

For this test case, we chose to specify the initial values of the conserved scalar ξ and the progress variable n in the fuel jet to represent the H_2 fuel. Thus, the fuel jet enters the mixing domain with

$\xi = 1$ and $n = 0.496$ (for the 22%Ar+78%hydrogen case, $n = 0.0965$) and with a temperature of 300 K. The stoichiometric conditions for the H_2-air combustion are given by $\xi_{st} = 0.028$ and $n_{st} = 0.0412$, and the flame temperature is 2193 K. For the 22%Ar+78%H_2-air combustion case, the stoichiometric conditions are given by $\xi_{st} = 0.1636$ and $n_{st} = 0.0388$ and the flame temperature is 2303 K. The air stream entrained into the mixing zone was assumed to be at a state given by $\xi = 0$ and $n = 0.03466$, and a temperature of 300 K. The effects of changing the fuel jet diameter, the fuel jet velocity, the spreading (and hence the entrainment) rate, and the location of entrainment were studied; only representative results are shown here (see Table III).

Figures 16a through 16d show, respectively, an instantaneous realization of the axial distribution of the scalar ξ, the progress variable n, the NO moles n_{NO} (both n and n_{NO} are in moles/unit mass) and the mixture density ρ (in kg/m^3) for a representative test case. For this simulation, a 0.52-cm diameter fuel jet enters the mixing region at a jet speed of 150 m/s and was modeled with the entrainment of air occurring over the entire axial extent with the free-jet spreading rate noted earlier. Figure 16a shows that the conserved scalar ξ starts with a value of 1 from the fuel jet (at $x/d_0 = 0$) but rapidly drops to low values as the air is entrained and combustion occurs. The progress variable n also shows a similar variation. Since both the mixture fraction and the progress variable were diffused and mixed identically, the variation in space at any given time is the same. The instantaneous variation of the NO moles, n_{NO}, shows that most of the local NO is produced around $x/d_0 = 65$. Finally, Figure 16d shows the density field at a given instant, indicating an increase in the density near the outflow. This increase is mainly due to the fact that most of the flow far downstream primarily contains air, which has a much higher density than H_2.

The axial variation of the species in the H_2-air reaction mechanism can also be determined for each of these test cases. Figures 17a through 17c show the axial variation (in moles/unit mass) of the species H_2O, H_2, O_2, H, O, OH, and HO_2 for a simulation which was similar to that shown in Figure 16 except that the fuel jet speed was 75 m/s. This configuration is similar to some experiments carried out in the past at Sandia Laboratories. To understand the mechanism of NO production and the variation of the different species in the mixing region, each of the parts of Figure 17 shows multiple plots for the various flow properties. For example, Figure 17a shows the temperature and the concentrations of O-atoms and NO molecules in the mixing region. Clearly, peak NO production occurs at the same location where temperature is also at a maximum. Since NO production requires the presence of O-atoms by virtue of the production mechanism, most of the NO is concentrated at the locations where O-atoms are present. As O-atoms are depleted, the NO production also decreases rapidly. Figure 17b shows how the other flow properties, for example, the concentration of H_2O, H_2, O_2, and OH, vary with axial distance. As combustion occurs, the H_2 concentration is depleted while the major product (water) begins to form and the temperature rises. The oxygen concentration increases in the far field due to the entrained air. The peak production of OH occurs close to the location of peak temperature. Thus, it appears all the radicals are located close to the peak temperature region. Finally, Figure 17c shows the concentrations of the rest of the species, H, OH, and HO_2 for this simulation. As the H_2 in the fuel jet breaks down H-atoms are formed much earlier; some of the H-atoms are combined with the available O-atoms to form OH near the peak temperature location. However, some of the H atoms are transported further downstream due to turbulent mixing to form HO_2 as can be seen in this figure.

Figures 18a and 18b show another simulation similar to that shown in Figure 17 except that, in this case, the fuel jet speed is doubled to 150 m/s. All conclusions discussed above for the lower jet speed case (Figure 17) hold again for this simulation. The only major difference is that the peak locations

appear to move slightly further downstream. To avoid causing confusion (due to the presence of multiple curves), the scales corresponding to the various flow properties are not shown in these two figures.

Figures 19a and 19b show the axial variation of the NO emission index for these two calculations. The emission index starts to increase at around $x/d_0 = 40$ for both cases and in the far field levels off. A similar trend has been observed in earlier H_2-air experiments. Note that with an increase in jet speed the emission index decreases. This also agrees with earlier experimental data (Chen and Driscoll, 1991), although a direct comparison is not possible since the conditions used in the present test case and those used in experiments are not the same. Furthermore, the present simulation has not been carried out for a sufficient long time to reach a statistically steady state. This can be seen because the length of the flame can be estimated from Figure 17a, by locating the downstream distance at which the mixture fraction becomes stoichiometric. The present simulation indicates a flame length of around $x/d_0 = 75$, which is less than the experimentally observed value.

Figures 20a and 20b show respectively, the scatter plot representation of $T-\xi$ variation with time at a given axial location of $x/d_0 = 30$. The general trend is very similar to earlier experiments as will be described further below.

Finally, a series of calculations was carried out using the 22%Ar-78%hydrogen flame combustion so that comparisons with earlier experiments (Magre and Dibble, 1988) and pdf computations (Chen and Kollman, 1990) could be carried out. Figures 25a through 25c show, respectively, the present computations, the experimental data of Magre and Dibble (1988), and the pdf computations of Chen and Kollmann (1990) in terms of the $T-\xi$ scatter at $x/d_0 = 30$ for fuel jet speed of 75 m / s. Figures 26 and 27 show, respectively, these three plots for the jet speeds of 150 and 225 m/s. Clearly, the present linear-eddy computations are capable of reproducing quite accurately the experimental and earlier pdf computed predictions. The increased scatter in the experimental data is due to the noise in the measurement, but the agreement between the present computations and these earlier works is quite remarkable.

Figure 24a shows a three-dimensional surface plot of the NO moles/unit mass n_{NO} as a function of the mixture fraction ξ and progress variable n for test case H-4. This figure clearly shows the allowable domain in the $n-\xi$ space where NO production occurs. It can be seen that peak production of NO occurs near stoichiometric conditions. Figure 24b shows another three-dimensional NO surface in the $T-\xi$ plane. NO is primarily produced at locations near stoichiometric conditions and at high temperatures. Finally, Figure 24c shows the variation of the NO Emission Index as a function of fuel jet speed. Also shown in this figure is the recent pdf prediction of Chen and Kollmann (1991). The linear-eddy prediction also shows the same trend, i.e., the NO Emission Index decreases with increasing jet velocity. However, the current predicted NO Emission Index does not agree with the pdf results for several reasons. The present calculation has not been carried out long enough to reach a statistically stationary state and, therefore, the present results do not indicate the final state in the mixture. Also, lack of time and resources also made it difficult to evaluate if the resolution used in the present calculation was sufficient. The pdf computations employed a surrounding coflowing air at a velocity of around 9.2 m/s (the linear-eddy calculations assumes that there is no coflowing air and the entrained air is initially at stagnant conditions). Finally, the specific geometry used in the pdf calculations was different (coaxial tubes) from the geometry modeled in the present study. All of these factors could contribute to the observed differences between the current computations and the past studies. However, the ability of the present mixing model to predict experimentally observed trends

(i.e., the decrease in emission index with jet speed) is very encouraging.

Finally, to demonstrate that the present model can predict experimentally observed values reasonably well, Figure 25 shows an earlier computation by Kerstein (1991a) for the H_2-air nonpremixed flame that was compared to some earlier data from Sandia. The reaction mechanism for this study was not the reduced-mechanism used here; an equilibrium assumption was used to relate all properties to the mixture fraction, as was done in the propane-air nonpremixed flame study described in this report. Clearly the capability of this mixing model to study realistic problems and its superiority over the instant mixing model have been established by the present study and by the earlier studies by Kerstein.

6. CONCLUSIONS AND RECOMMENDATIONS

In this report, the development of a new mixing model is described that takes into account the fundamental features of turbulent mixing. Both turbulent mixing and molecular diffusion in the small scales have been identified in experiments to be important in flows with chemical species. By specifically separating these two effects and modeling them in the small scales, the mixing model developed here has a capability that all previous mixing models have lacked. This mixing model was used to study multispecies mixing, a propane-air nonpremixed flame, and a hydrogen-air nonpremixed flame. Since these three test cases required different model formulations, the capability of the mixing model to handle all three different test cases clearly show its potential for wide application. The production of NO due to a thermal mechanism (the Zeldovich mechanism) was also estimated in all three cases, and the effects of jet diameter, jet speed, and modification of the turbulent mixing and air entrainment process were studied. Due to resource limitations, a parametric study has not yet been carried out; however, the series of calculations shown in this report indicates that a parametric study can easily be accomplished.

Comparison of the present results with experimental data and the earlier comparisons by Kerstein (1991a) clearly demonstrate the strengths of the linear-eddy model. The present study has shown that finite-rate kinetics in the form of a reduced-mechanism can easily be incorporated within the framework of the mixing model. The work carried out so far has provided enough understanding of the behavior of the mixing model and has laid the basic framework for application to practical design problems, which will be studied in the next phase.

In the next phase (a proposal will be submitted), we propose to further improve the model and implement it in a manner that would provide a numerical capability to address practical issues such as the mixing process in the quench zone of the RQL combustor. Issues regarding the grid resolution, the time of simulation, and the mixing geometry will be addressed first. Then, a series of parametric studies will be carried out with the present code to determine the importance of the various time and length scales that were identified in the Phase I study.

In parallel to this parametric study, a major research effort will be undertaken in which the present mixing model will be coupled to a steady-state prediction code. The steady-state code will not be developed. Two possible options are currently viable. The first approach is to couple the mixing model to a standard finite-difference steady-state code using the $k - \epsilon$ turbulence model. The second approach is to couple the present mixing model to a prediction code based on the pdf method for the joint-scalar pdf or the joint-velocity-scale pdf. The linear-eddy model has many elements that are also present in the Monte Carlo approach used in pdf methods. Therefore, it is possible to implement this model within the pdf method to account for the unsteady mixing effects. The second approach (coupling the mixing model to the pdf method) may be, in the long run, more productive, since the pdf method is superior to the standard finite-difference method. The basic weakness of the current pdf codes is in the mixing model (typically, mixing models similar to Curl's mixing model is used) and, therefore, the strength of the present linear-eddy model could be used to enhance the pdf method's capability. Of course, to couple the present mixing model to the pdf method will require access to the code. Pdf codes are used in General Electric and General Motors research groups (private communications); however, these codes are not in the public domain. We will discuss the issues involved in coupling the mixing model to steady-state codes in more detail in the Phase II proposal.

Implementation of the present model within the framework of a standard finite-difference code or a pdf code will require significant modifications to the present model (particularly the application-specific elements described in Section 3.2). For example, if this mixing model is used in a standard finite-difference code, then instead of using the discretization shown in Figure 2 for the entire mixing region, the mixing model will be implemented within each grid cell as shown in Figure 26. Computations of turbulent mixing, molecular diffusion and chemical heat release can then be carried out within each cell as described in Sections 3.1 and 3.3. Large-scale transport due to the mean flow and turbulent fluctuations primarily due to the volume fluxes from the neighboring cells, will result in changes to the flow properties in each cell. The exchange of species between neighboring cells will have to be taken into account. All these processes will result in a new state of the species, temperature, and density field within each grid cell. By Favre-averaging these properties within the linear eddies in each cell, the new mean properties can be determined and can then be used to correct the mean mass, momentum, and energy transport being computed in the steady-state algorithm. A technique for modeling the exchange between neighboring cells and a method for coupling the effects of small scale mixing and combustion to the Navier-Stokes equations (mass, momentum, and energy equations) have recently been developed (Menon, 1991; Menon et al., 1991; McMurtry et al., 1992) within the framework of a subgrid model approach. Therefore, the specific method for coupling the present model to standard codes has already been developed. The coupling issues will be will be discussed in more detail in the Phase II proposal.

Finally, the physical problem discussed in this report is the mixing process and NO formation in the quench zone of the RQL combustor. However, from the formulation described in this report, it should be clear that the present model is not restricted to that mixing geometry and could be used for other flows. If the quench zone of the RQL combustor is modeled, then to study the mixing problem, the inflow to the mixing model (i.e., the exit conditions from the primary stage) must be provided from some steady-state prediction. However, if the original steady-state prediction of the state of the flow in the primary stage is in error (a serious possibility), then even if the present model is accurate, its predictions will be contaminated by the errors in the original input. A more practical approach would be to use the present model within the framework of a steady-state code to first predict the flow properties in the primary stage before addressing the quench zone. All these issues will be discussed in more detail in the Phase II proposal.

ACKNOWLEDGEMENT

The research described in this report would not have been possible without the enthusiastic encouragement from Dr. Alan R. Kerstein of Sandia National Laboratories, Livermore, California. Discussions with him proved invaluable in solving many problems encountered during the course of this research. Dr. J.-Y. Chen, also of Sandia, provided the original reduced-mechanism code and his help to incorporate the reduced mechanism within the mixing model is gratefully acknowledged. Finally, Dr. Patrick McMurtry of the University of Utah played a major role in the formulation and implementation of this mixing model.

REFERENCES

Bahr, D. W. (1980) "Gas Turbine Engine Emission Abatement - Status and Needed Advancements," in *Gas Turbine Combustor Design Problems* (ed. A. H. Lefebvre), Hemisphere Pub. Corp., New York.

Barlow, R. S., Dibble, R. W., Chen, J.-Y., and Lucht, R. P. *Combustion and Flame*, Vol. 82, pp. 235-291.

Becker, H. A., and Yamazaki, S. (1978) "Entrainment, Momentum Flux and Temperature in Vertical Free Turbulent Diffusion Flames," *Combustion and Flame*, Vol. 33, pp. 123-149.

Butler, G. W., and Pratt, D. T. (1986) "Coalescence/Dispersion Modeling of Turbulent Combustion in a Jet-Stirred Reactor," *AIAA J.*, Vol. 24, pp. 1817-1822.

Chen, J.-Y., and Dibble, R. W. (1990) "Application of Reduced Chemical Mechanisms for Prediction of Turbulent Nonpremixed Methane Jet Flames," Sandia National Laboratories Report SAND90-8447, February.

Chen, J.-Y., and Kollmann, W. (1990) "Chemical Models for Pdf Modeling of Hydrogen-Air Nonpremixed Turbulent Flames," *Combustion and Flame*, Vol. 79, pp. 75-99.

Chen, J.-Y., and Kollmann, W. (1991) "Pdf Modeling and Analysis of Thermal NO Formation in Turbulent Nonpremixed Hydrogen-Air Jet Flames," submitted to *Combustion, Science and Technology*.

Chen, H.-H., and Driscoll, J. F. (1990) "Nitric Oxide Levels of Jet Diffusion Flames: Effects of Coaxial Air and Other Mixing Parameters," 23rd Symposium (Intn.) on Combustion, pp. 281-288.

Cooper, L. P. (1979) "The Effect of Degree of Fuel Vaporization Upon Emissions for a Premixed, Prevaporized Combustion System," AIAA-79-1320.

Correa, S. M. (1984) "Prediction of an Axisymmetric Combusting Flow," *AIAA J.*, Vol. 22, pp. 1602-1608.

Correa, S. M., and Shyy, W. (1987) "Computational Models and Methods for Continuous Gaseous Turbulent Combustion," in *Prog. Energy Combust. Sci.*, Vol. 13, pp. 249-292.

Curl, R. L. (1963) "Dispersed Phase Mixing: I. Theory and Effects in Simple Reactors," *AIChE J.*, Vol. 9, pp. 175-181.

Dahm, W. J. A., and Dimotakis, P. E. (1987) "Measurements of Entrainment and Mixing in Turbulent Jets," *AIAA Journal*, Vol. 25, pp. 1216-1223.

Dimotakis, P. E. (1989) "Turbulent Free Shear Layer Mixing," AIAA-89-0262.

Drake, M. C., Correa, S. M., Pitz, R. W., Shyy, W., and Fenimore, C. P. (1987) "Superequilibrium and Thermal Nitric Oxide Formation in Turbulent Diffusion Flames," *Combust. Flame*, Vol. 69, pp. 347-365.

Janicka, J., and Kollmann, W. (1982) *Combustion and Flame*, Vol. 44, pp. 319-336.

Kerstein, A. K. (1988) "Linear-Eddy Model of Turbulent Scalar Transport and Mixing," *Comb. Sci. and Tech.*, Vol. 60, pp. 391-421.

Kerstein, A. K. (1989) "Linear-Eddy Modeling of Turbulent Transport II: Application to Shear Layer Mixing," *Comb. and Flame*, Vol. 75, pp. 397-413.

Kerstein, A. K. (1990) "Linear-Eddy Modeling of Turbulent Transport. III: Mixing and Differential Molecular Diffusion in Round Jets," *J. Fluid Mech.* (in press).

Kerstein, A. K. (1991a) "Linear-Eddy Modeling of Turbulent Transport. Part 4: Diffusion-Flame Structure", submitted to *Combustion Science and Technology*.

Kerstein, A. K. (1991b) "Linear-Eddy Modeling of Turbulent Transport. Part 5: Geometry of Scalar Interfaces," *Phys. Fluids A.*, Vol. 3, Pt.2, pp. 1110-1114.

Magnussen, B. F., and Hjertager, B. H. (1977) "On Mathematical Modeling of Turbulent Combustion with Special Emphasis on Soot Formation and Combustion," *16th Symp. (Int.) on Comb.*, pp. 719-729.

Magre, P., and Dibble, R. W. (1988) *Combustion and Flame*, Vol. 73, pp. 195-206.

McMurtry, P, Menon, S. and Kerstein, A. (1992) "A New Subgrid Model for Turbulent Mixing and Reactions," AIAA Paper No. 92-0234, to be presented at the AIAA 30th Aerospace Sciences Meeting, Reno, NV, January.

McVey, J. B., and Kennedy, J. B. (1979) "Lean Stability Limit Augmentation for Premixing Prevaporizing Combustors," AIAA-79-1319.

Menon, S. (1991) "A New Subgrid Model for Large-Eddy Simulations of Mixing and Chemical Reaction in Turbulent Flows," Final Report under Contract No. NAS2-13354, NASA Ames Research Center.

Menon, S., McMurtry, P., Kerstein, A. and Chen, J.-Y. (1992) "A Mixing Model to Predict NOx Production During Rapid Mixing in a Dual Stage Combustor," AIAA Paper No. 92-0233, to be presented at the AIAA 30th Aerospace Sciences Meeting, Reno, NV, January.

Menon, S., McMurtry, P., and Kerstein, A. (1991) "A Linear Eddy Flamelet Subgrid Model for Large-Eddy Simulations of Turbulent Premixed Combustion," to be presented at the 4th International Conf. on Numerical Combustion, St. Petersburg, FL, Dec 2-4.

Mularz, E. J. (1979) "Lean, Premixed, Prevaporized Combustion for Aircraft Gas Turbine Engines" AIAA-79-1318.

Mungal, M. G., and Hollingsworth, D. K. (1989) "Organized Motion in a Very High Reynolds Number Jet," *Phys. Fluids A*, Vol. 1, pp. 1615-1623.

Mungal, M. G., and O'Neil, J. M. (1989) "Visual Observation of a Turbulent Jet Diffusion Flame," *Combust. Flame*, Vol. 78, pp. 377-389.

Nguyen, L. H., and Bittker, D. A. (1989) "Investigation of Low NOx Staged Combustor Concept in High-Speed Civil Transport Engines," NASA TM 101977, July.

Ott, J. (1990) "Researchers Seek Technologies for Quiet, Environmentally Safe SST," *Aviation Week and Space Technology*, June 18, pp. 94-98.

Peters, N., and Donnerhack, S. (1981) "Structure and Similarity of Nitric Oxide Production in Turbulent Diffusion Flames," *18th Symp. (Int.) on Combustion*, The Combustion Institute, pp. 33-42.

Pope, S. B., and Correa, S. M. (1986) "Joint PDF Calculations of a Non-equilibrium Turbulent Diffusion Flame," in *21st Symp. (Int.) on Combustion.*

Pratt, D. T. (1980) "Coalescence/Dispersion Modeling of Gas Turbine Combustors," in *Gas Turbine Combustor Design Problems* (ed. A. H. Lefebvre), Hemisphere Publishing Co., New York.

Ricou, F. P., and Spalding, D. B. (1961) "Measurements of Entrainment by Axisymmetrical Turbulent Jets," *J. Fluid Mech.*, Vol. 11, pp. 21-32.

Semerjian, H. G., Ball, I. C., and Vranos, A. (1979) "Pollutant Emissions from 'Partially' Mixed Turbulent Flames," *Proc. 17th Int. Symp. on Combustion*, pp. 679-687.

Swithenbank, J., Turan, A. and Felton, P. G. (1980) "Three-Dimensional Two-Phase Mathematical Modeling of Gas Turbine Combustors," in *Gas Turbine Combustor Design Problems* (ed. A. H. Lefebvre), Hemisphere Publishing Co., New York.

Tacina, R. R. (1990) "Low NOx Potential of Gas Turbine Engines," AIAA-90-0550.

Tang, S. K., and Churchill, S. W. (1981) "The Formation of Thermal and Fuel NOx for Radially Stabilized Combustion," *Proc. 18th Int. Symp. on Combustion*, pp. 73-80.

Warnatz, J., (1984) in *Combustion Chemistry* (W. C. Gardiner Jr., Ed.), Springer-Verlag, Berlin, pp. 197.

Westmoreland, J. S., Howlett, R. A., and Lohmann, R. P. (1979) "Progress on Variable Cycle Engines," AIAA-79-1312.

Table I. Multispecies Mixing Test Cases

Test Case	Jet Vel (m/s)	Jet Temp °K	Jet Dia. (m)	Jet Species at x = 0	Jet Initial Cond.	Air Temp °K	Air Species	Comments
M-1	12	2100	0.046	Set A	Condition A	300	N_2, O_2	L(x) = 1 + 0.05x, pure mixing, no NO production
M-2	12	2100	0.046	Set A	Condition A	300	N_2, O_2	L(x) = 1 + 0.05x, no mixing, no air entrainment for $x/d_0 < 13$; no NO production
M-3	12	1200	0.046	Set A	Condition A	300	N_2, O_2	L(x) = 1 + 0.05x, no mixing, no air entrainment for $x/d_0 < 13$, NO production (Peters and Donnerhack, 1981)
M-4	12	2100	0.01	Set A	Condition B	300	N_2, O_2	L(x) = 1 + 0.14x, NO production (Peters and Donnerhack, 1981)
M-5	12	2000	0.01	Set B	Condition C	1100	N_2, O_2	L(x) = 1 + 0.14x, pure mixing case: representative of RQL quench zone inflow (Howe et al., 1991)

Set A = N_2, O_2, O, N, NO

Set B = O_2, N_2, H_2O, CO, C_3H_8

Condition A: $Y_{N_2} = 0.2$, $Y_{O_2} = 0.6$, $Y_O = 0.1$, $Y_N = 0.05$, $Y_{NO} = 0.05$

Condition B: $Y_{N_2} = 0.0$, $Y_{O_2} = 0.6$, $Y_N = 0.1$, $Y_O = 0.3$, $Y_{NO} = 0.0$

Condition C: $Y_{O_2} = 0.0$, $Y_{N_2} = 0.6925$, $Y_{H_2O} = 0.1354$, $Y_{CO} = 0.1578$, $Y_{C_3H_8} = 0.0143$

Table II. Propane-Air Nonpremixed Flame Test Cases

	Fuel Jet Conditions			
Test Case	Vel (m/s)	Temp T/T_a	Density (ρ/ρ_a)	Dia (m)
P-1	12	7.61	1.526	0.0039
P-2	24	7.61	1.526	0.0039
P-3	48	7.61	1.526	0.0039
P-4	72	7.61	1.526	0.0039

Table III. Hydrogen-Air Nonpremixed Flame Test Case

	Fuel Jet Conditions				Stoichiometry Conditions			Comments
Test Case	Vel (m/s)	Temp °K	Dia. (m)	x = 0 Initial Cond	η_{stoic}	ξ_{stoic}	T_{stoic} (°K)	
H-1	75	300	0.005	$\xi = 1$ $\eta = 0.496$	0.0412	0.028	2193	L = 1 + 0.14x, H_2-air combustion; reduced mechanism
H-2	150	300	0.005	$\xi = 1$ $\eta = 0.496$	0.0412	0.028	2193	L = 1 + 0.14x, H_2-air combustion; reduced mechanism
H-3	75	300	0.0052	$\xi = 1$ $\eta = 0.0965$	0.0388	0.1632	2303	L = 1 + 0.14x, 22% Ar + 78% H_2-air combustion; reduced mechanism
H-4	150	300	0.0052	$\xi = 1$ $\eta = 0.0965$	0.0388	0.1632	2303	L = 1 + 0.14x, 22% Ar + 78% H_2-air combustion; reduced mechanism
H-5	225	300	0.0052	$\xi = 1$ $\eta = 0.0965$	0.0388	0.1632	2303	L = 1 + 0.14x, 22% Ar + 78% H_2-air combustion; reduced mechanism

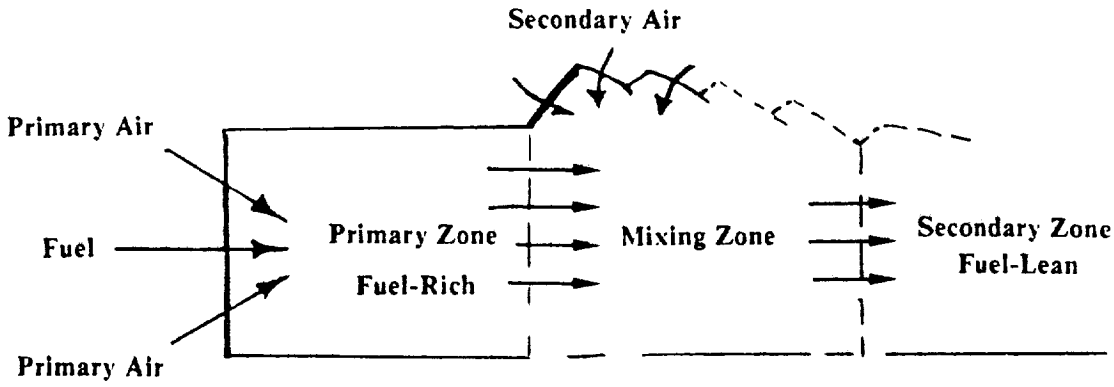

Figure 1. Idealized RQL combustor

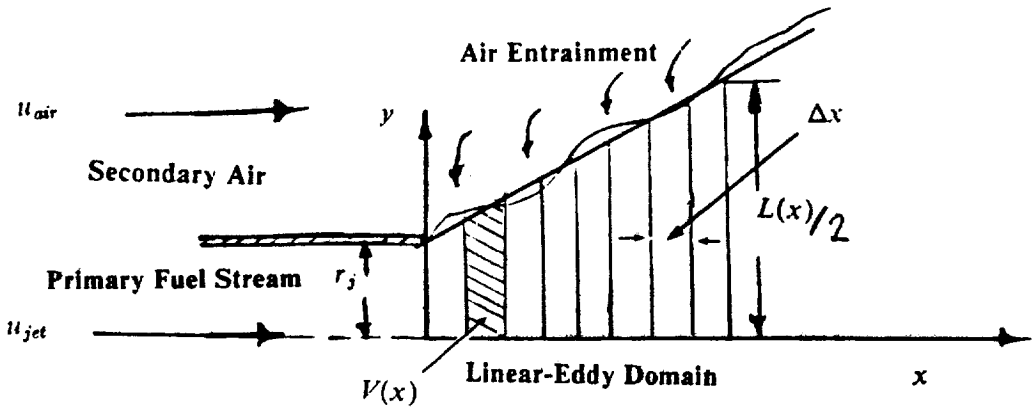

Figure 2. Mixing region downstream of a fuel jet

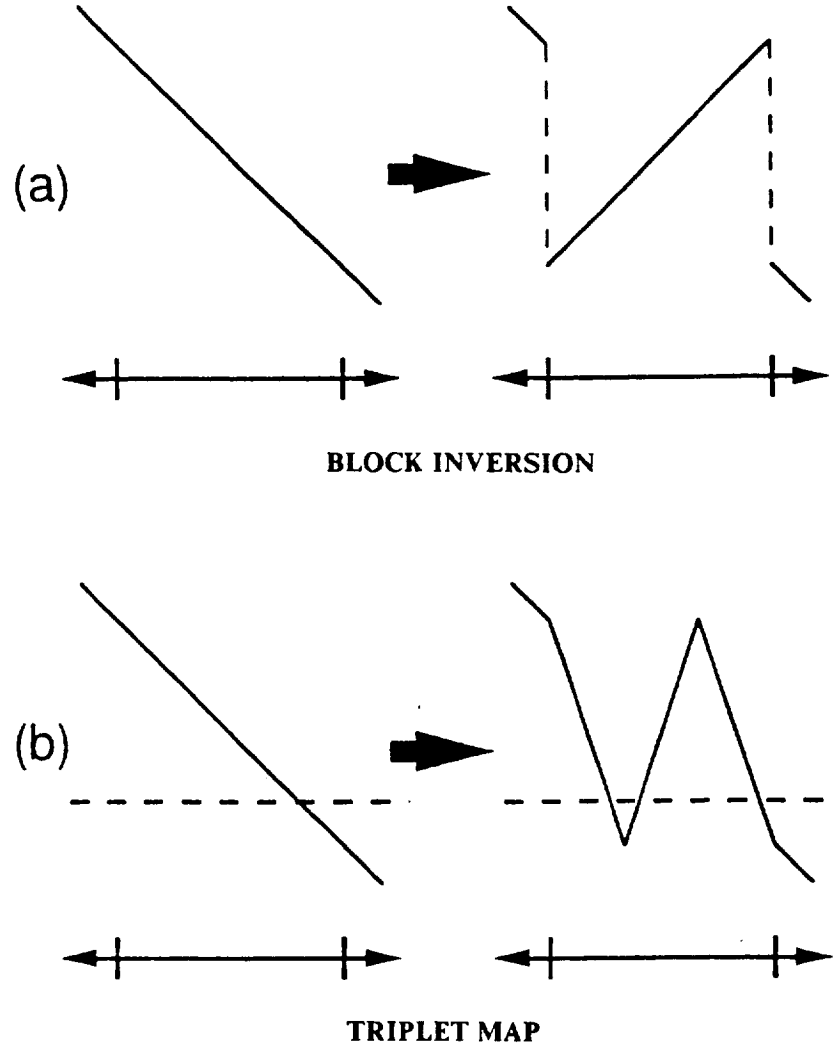

Figure 3. Alternative rearrangement processes representing the effect of individual turbulent eddies. In each panel, the double-arrowed line represents the spatial domain. Tick marks demarcate a segment selected for rearrangement. For the purpose of this illustration, the concentration field prior to rearrangement is taken to be linear in the spatial coordinate. Block inversion (a), employed in previous applications, introduces two discontinuities in the concentration field, indicated by the vertical dashed lines. The triplet map (b), adopted in the present formulation, introduces no discontinuities, though it introduces discontinuous derivatives. It triples the number of level crossings of any concentration value within the segment (e.g., crossings of the value represented by the horizontal dashed line), corresponding to a tripling of area of any material surface within the segment. **(From Kerstein, 1991a)**

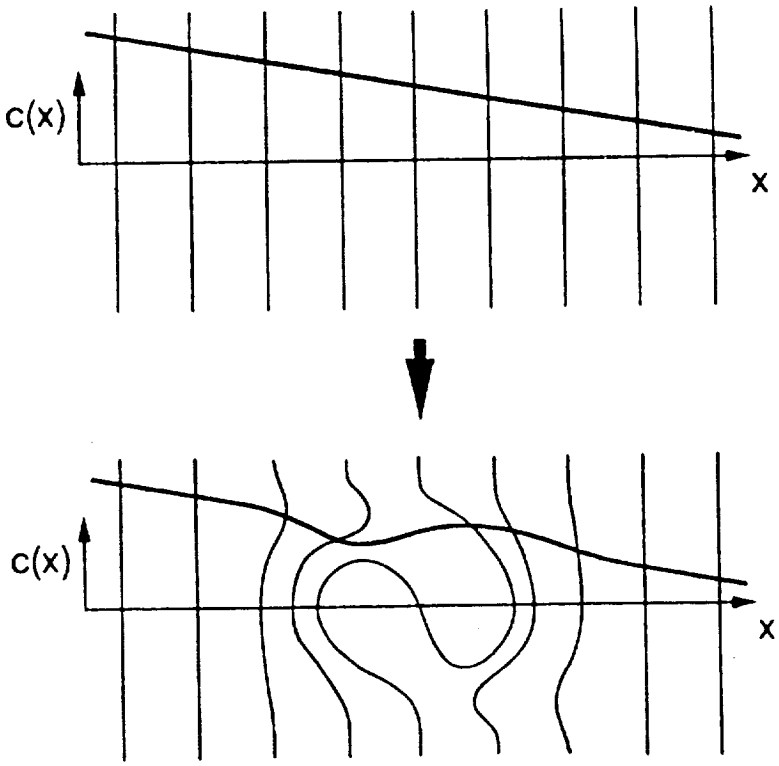

Figure 4. Schematic illustration of the effect of a single, clockwise eddy on a two-dimensional scalar field that initially has a uniform concentration gradient. Upper panel: initial concentration isopleths (vertical lines) and concentration profile $c(x)$ (heavy line) parallel to the initial concentration gradient. Lower panel: concentration isopleths and concentration profile at a later time. **(From Kerstein, 1991a)**

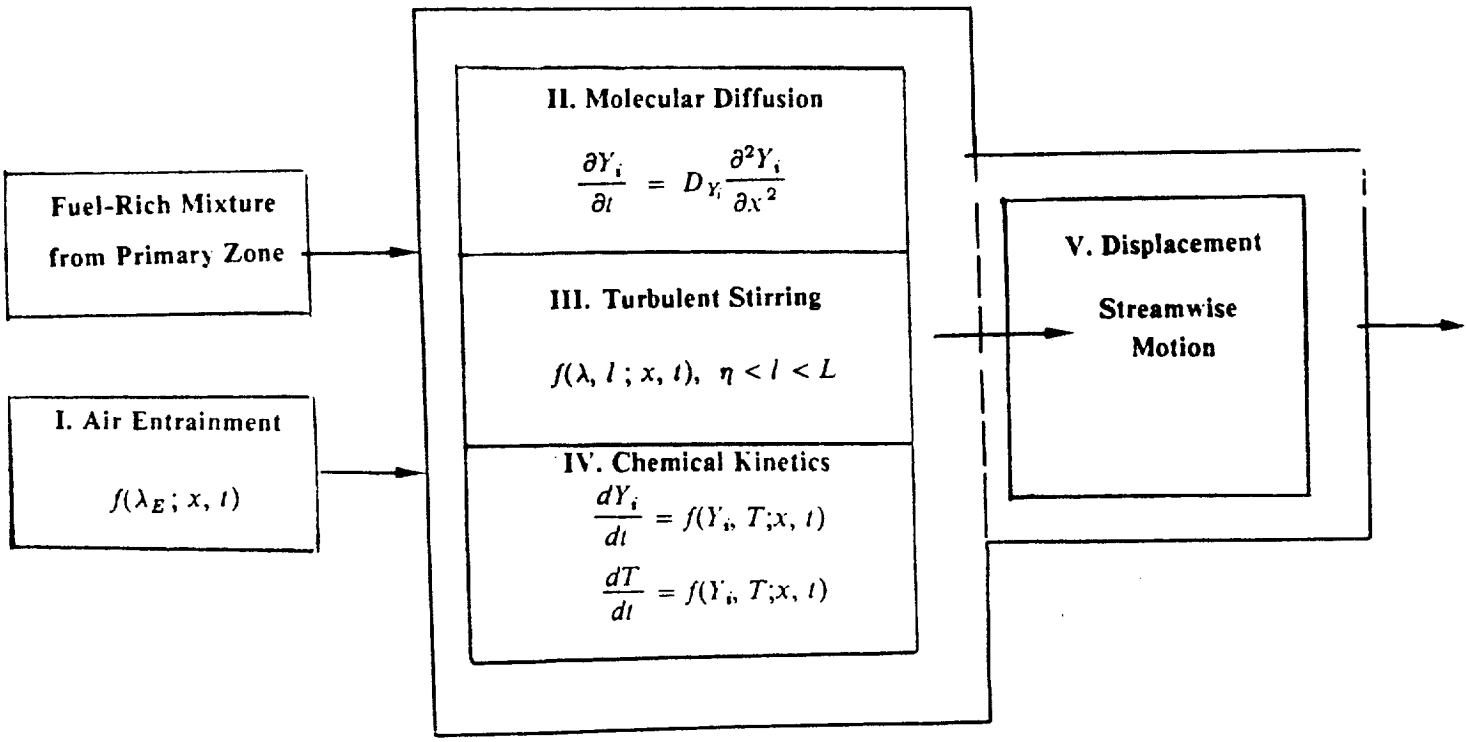

Figure 5. Block schematic of the linear-eddy algorithm

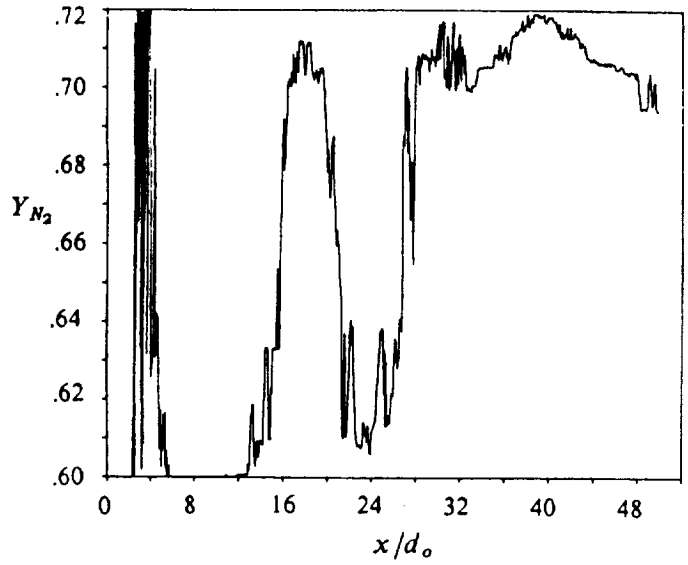

a. Nitrogen mass fraction (Y_{N_2})

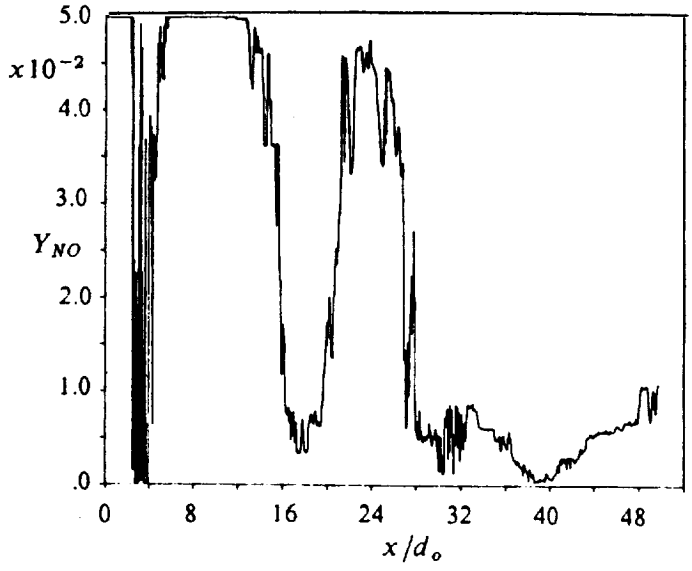

b. Nitric oxide mass fraction (Y_{NO})

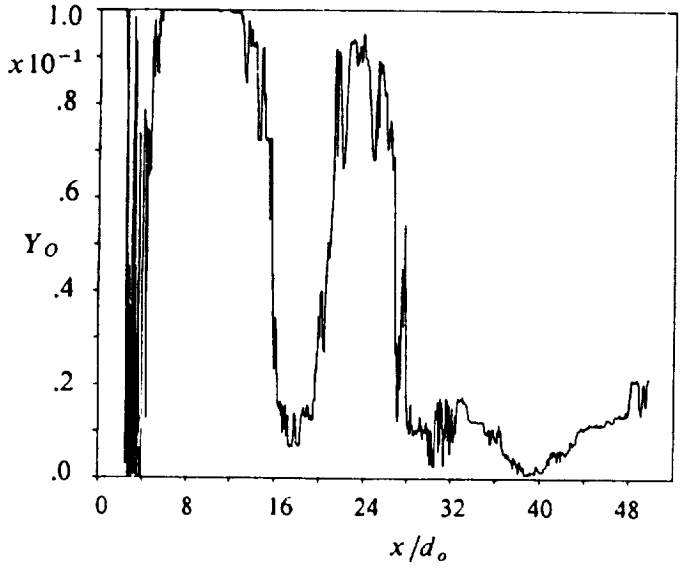

c. Oxygen atom mass fraction (Y_O)

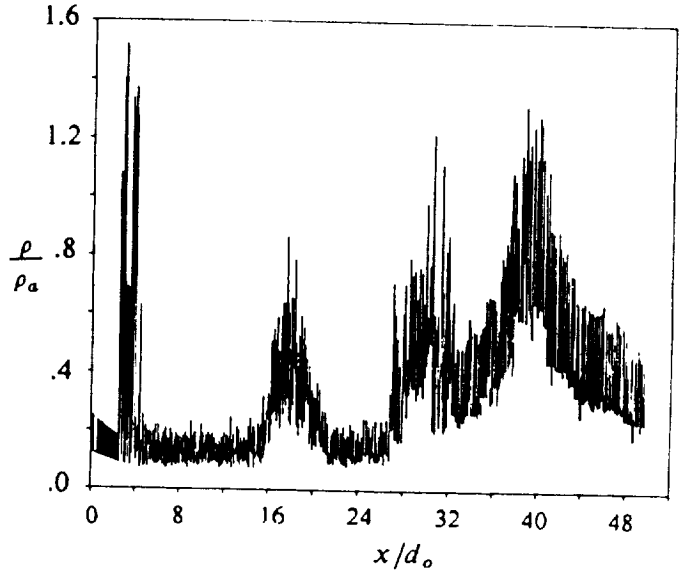

d. Density (ρ/ρ_a)

Figure 6. Axial variation of the species and flow properties during multispecies mixing. Test condition M-1 (see Table I).

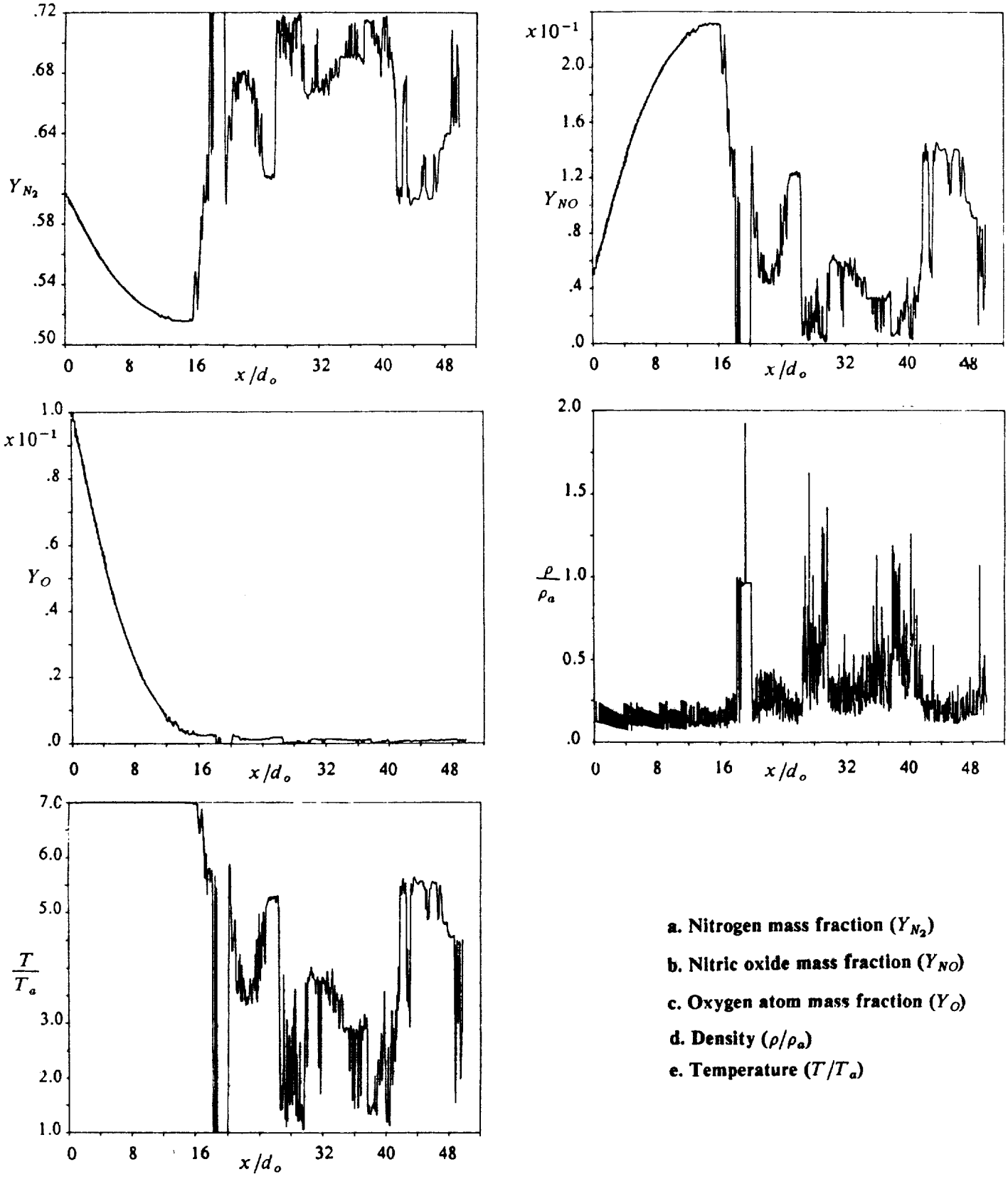

a. Nitrogen mass fraction (Y_{N_2})

b. Nitric oxide mass fraction (Y_{NO})

c. Oxygen atom mass fraction (Y_O)

d. Density (ρ/ρ_a)

e. Temperature (T/T_a)

Figure 7. Axial variation of the species and flow properties during multispecies mixing. Test condition M-3 (see Table I).

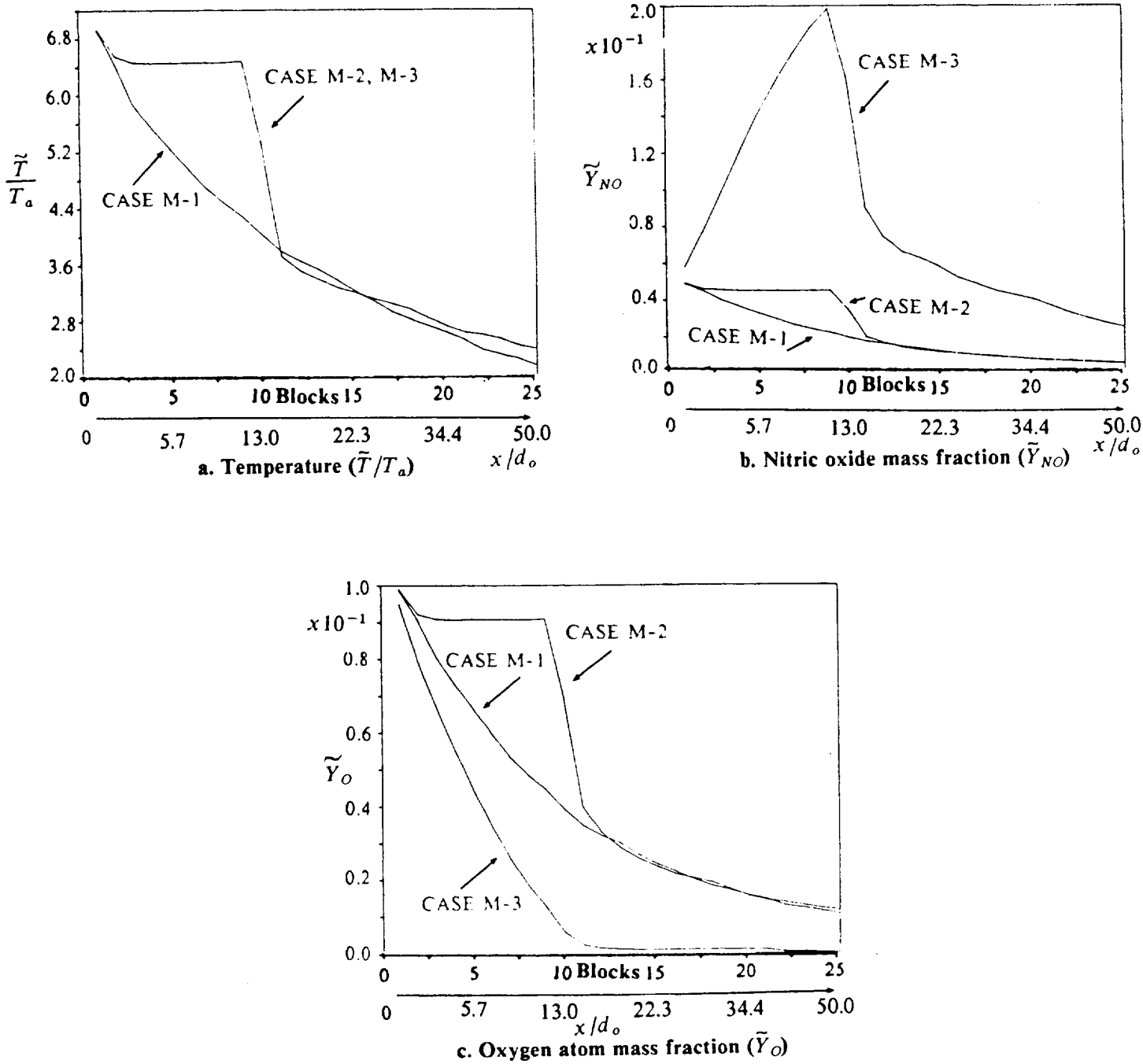

Figure 8. Axial variation of Favre-averaged flow properties for test cases M-1, M-2 and M-3.

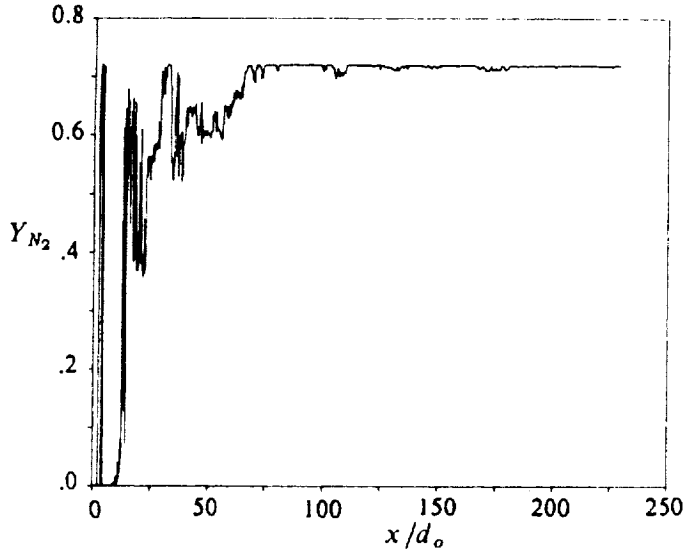

a. Nitrogen mass fraction (Y_{N_2})

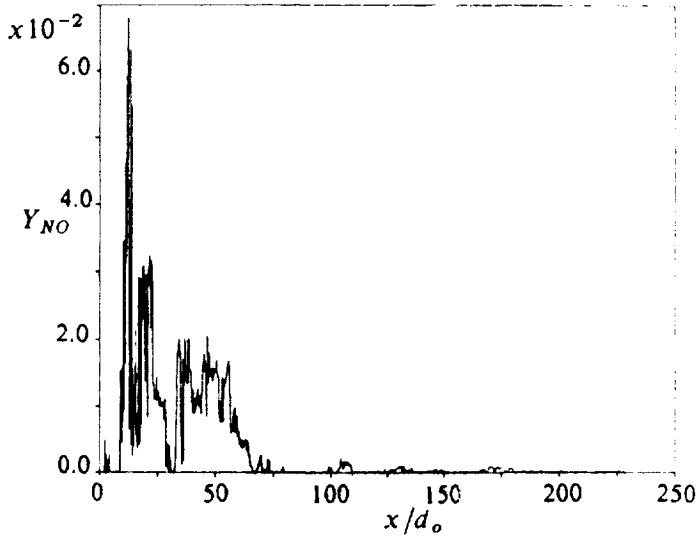

b. Nitric oxide mass fraction (Y_{NO})

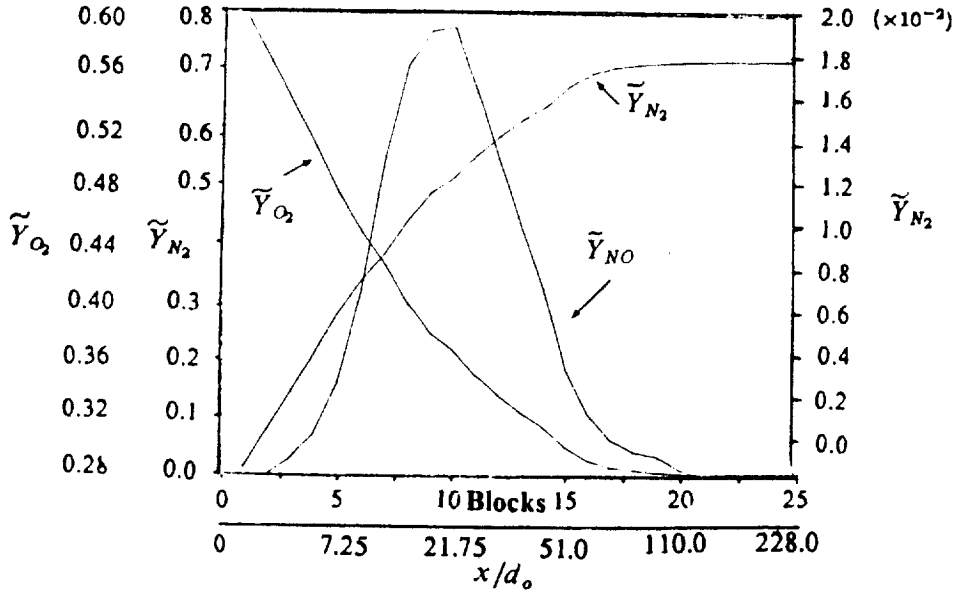

c. Axial variation of Favre-averaged flow properties.

Figure 9. Axial variation of the species and flow properties during multispecies mixing. Test condition M-4 (see Table I).

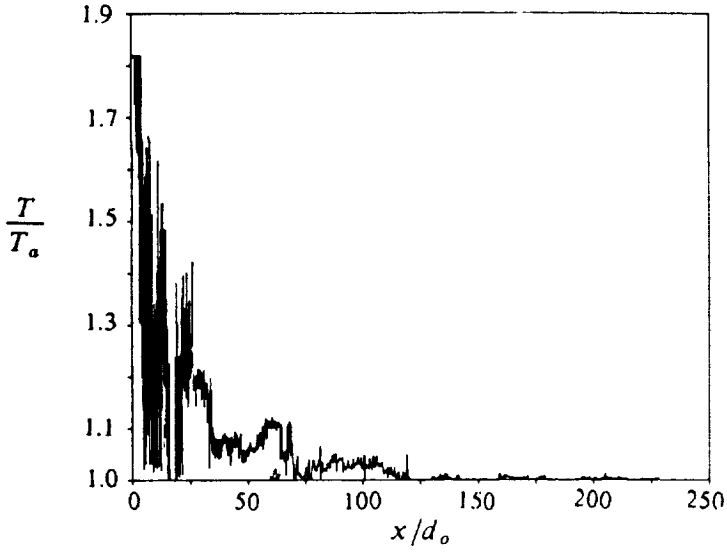

a. Temperature (T/T_a)

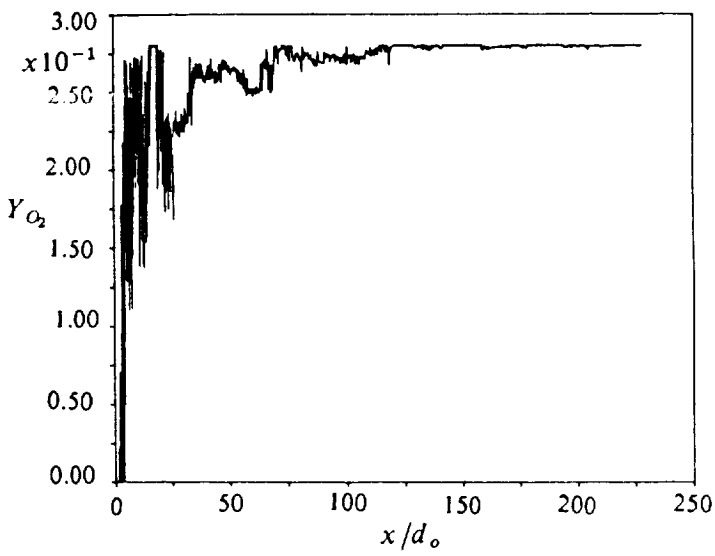

a. Oxygen mass fraction (Y_{O_2})

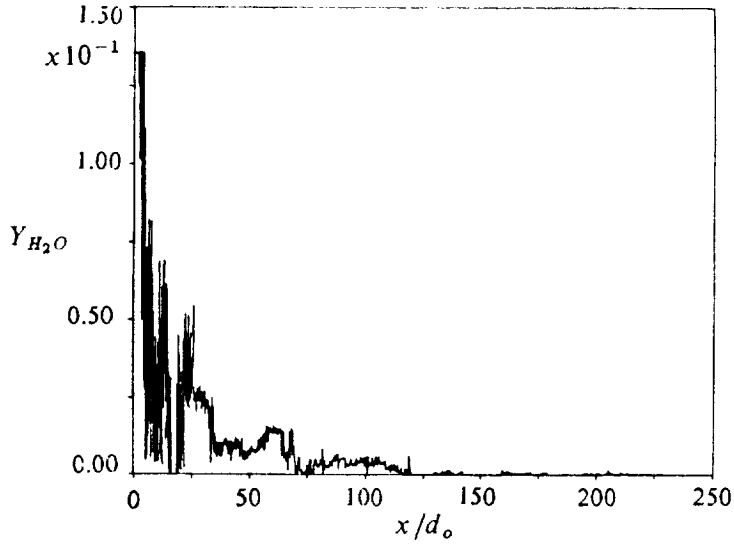

b. Water mass fraction (Y_{H_2O})

Figure 10. Axial variation of the species and flow properties during multispecies mixing. Test condition M-5 (see Table I).

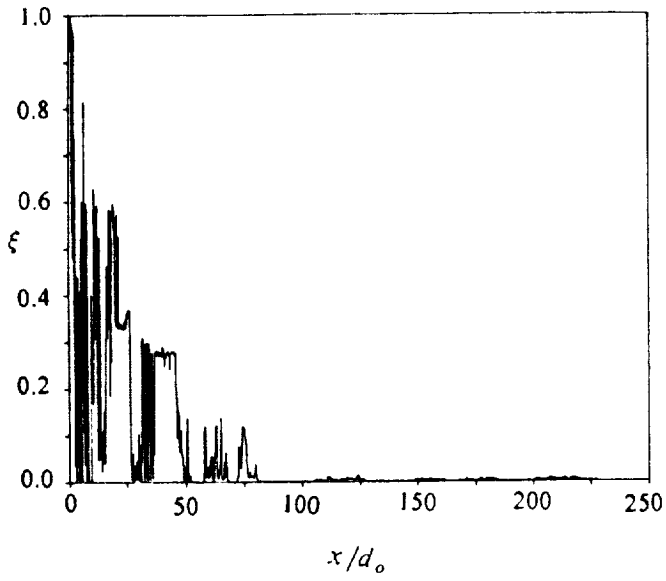

a. Mixture fraction (ξ)

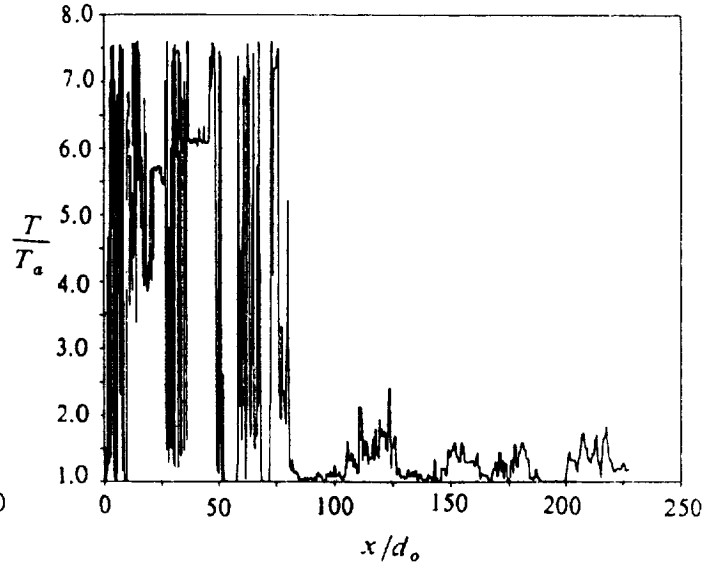

b. Temperature (T/T_a)

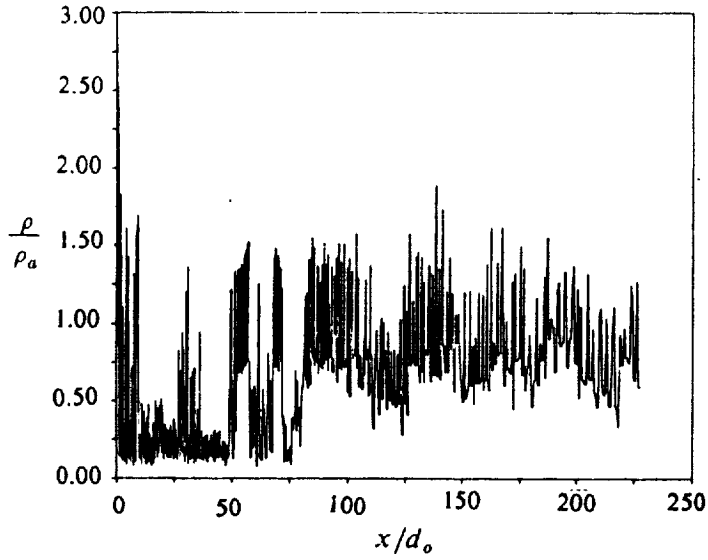

c. Density (ρ/ρ_a)

Figure 11. Axial variation of flow properties in the mixing region during propane-air combustion. Test condition P-1 (see Table II).

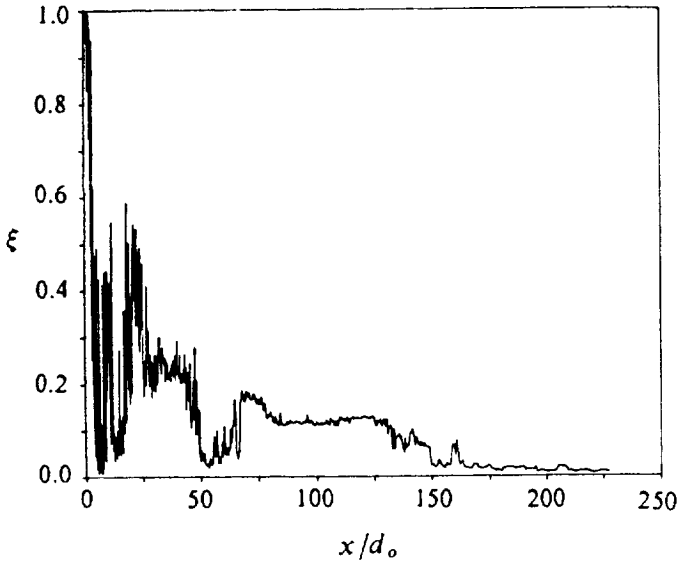

a. Mixture fraction

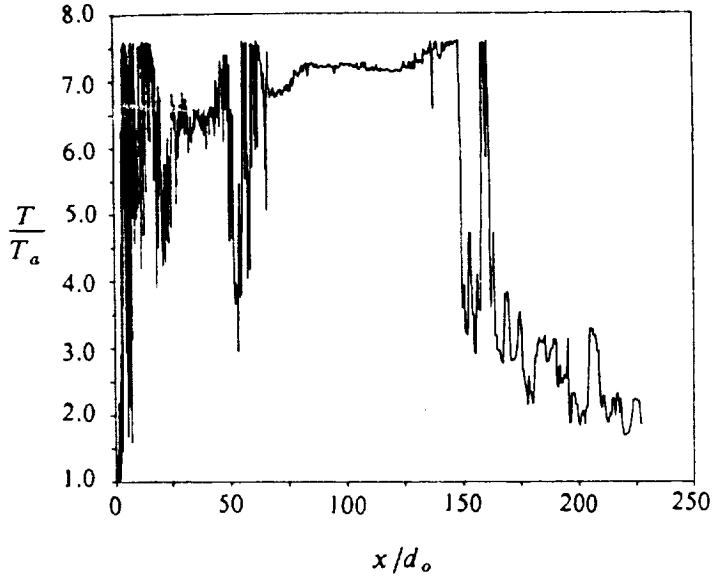

b. Temperature

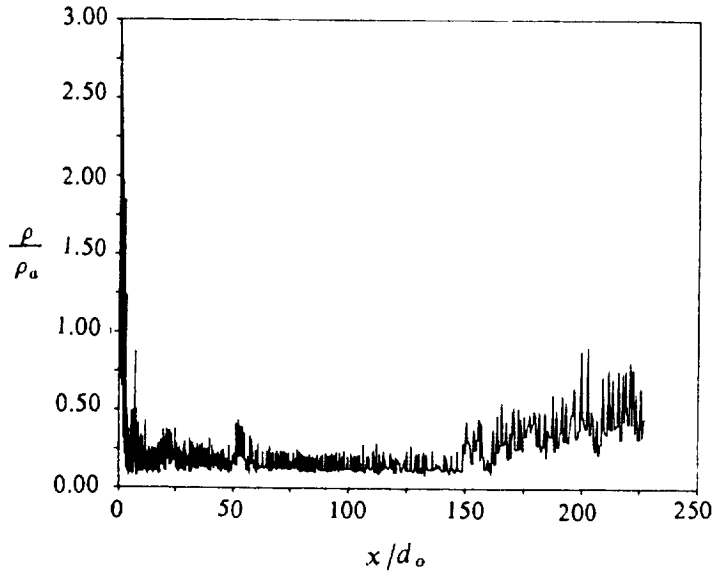

c. Density

Figure 12. Axial variation of flow properties in the mixing region during propane-air combustion. Test condition P-4 (see Table II).

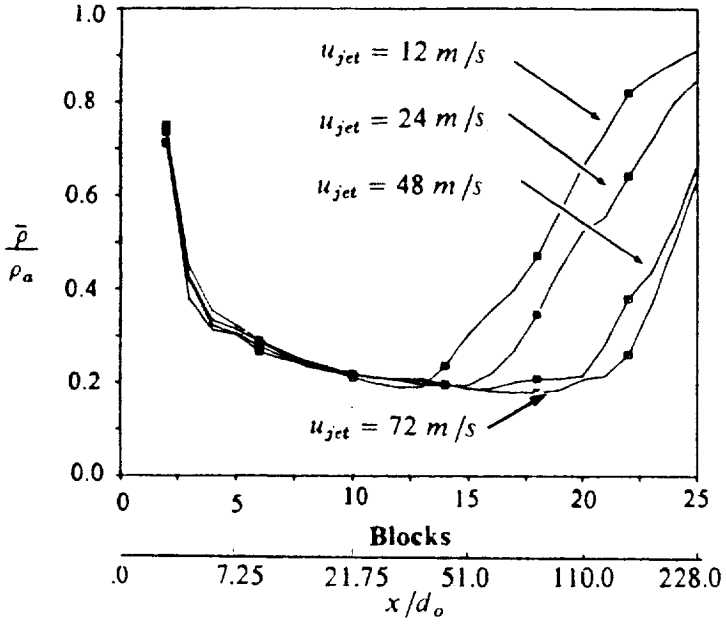

a. Density variation with fuel jet speed

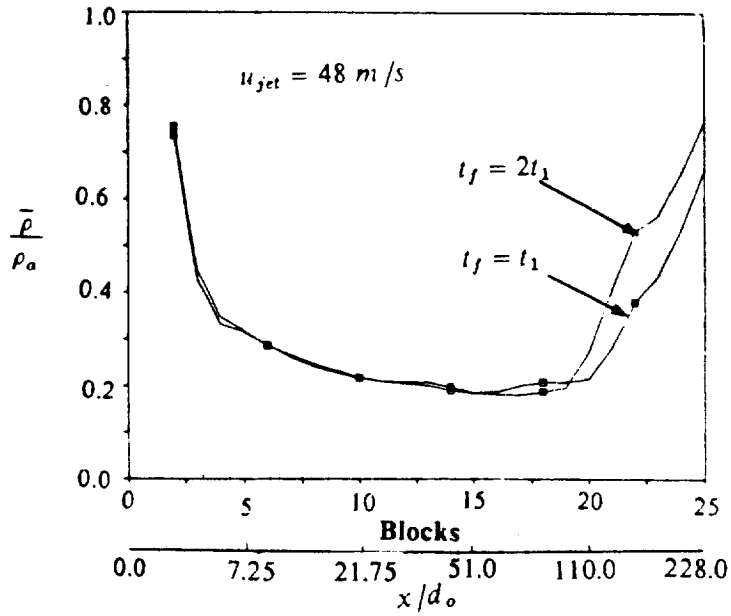

b. Density variation with time of simulation

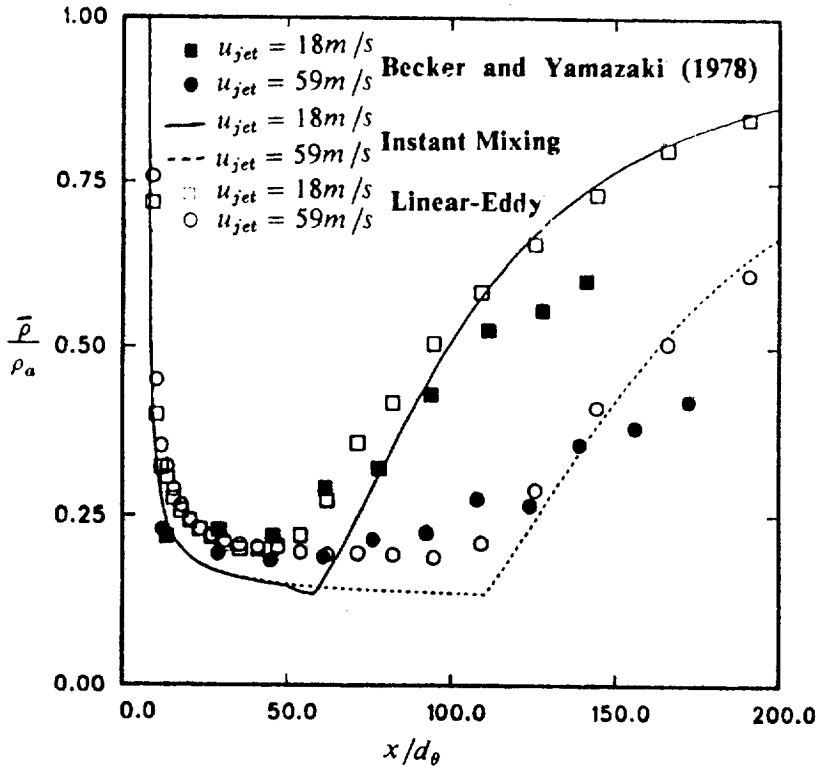

c. Comparison of computed and experimental axial density variation (Kerstein, 1991a)

Figure 13. Axial variation of time-averaged non dimensional density (ρ/ρ_a) during propane-air combustion for various test cases.

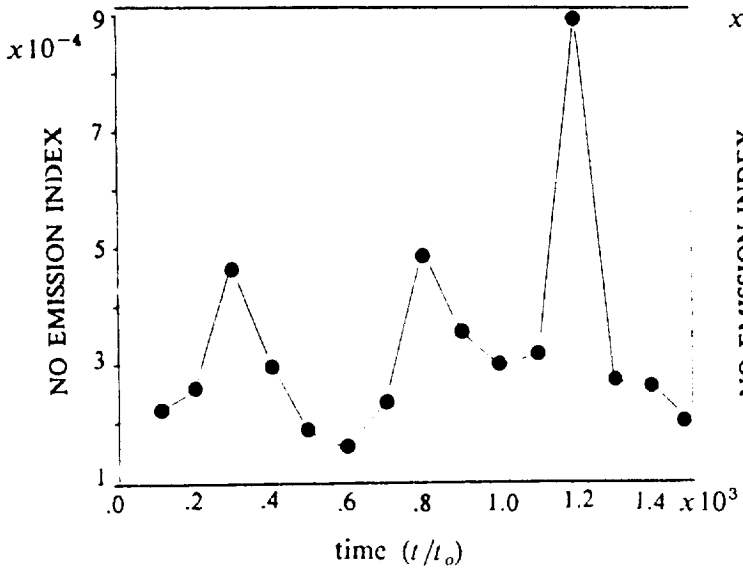

a. NO Emission Index for test case P-1 (u_{jet} = 12 m/s)

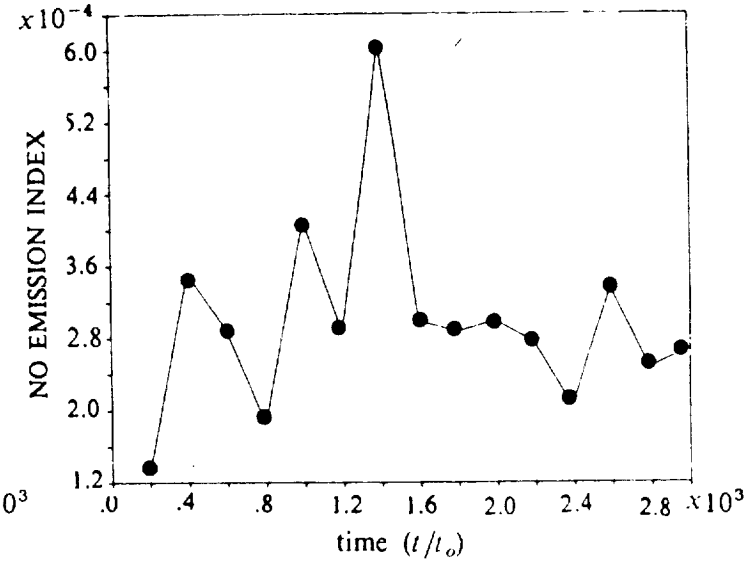

b. NO Emission Index for test case P-2 (u_{jet} = 24 m/s)

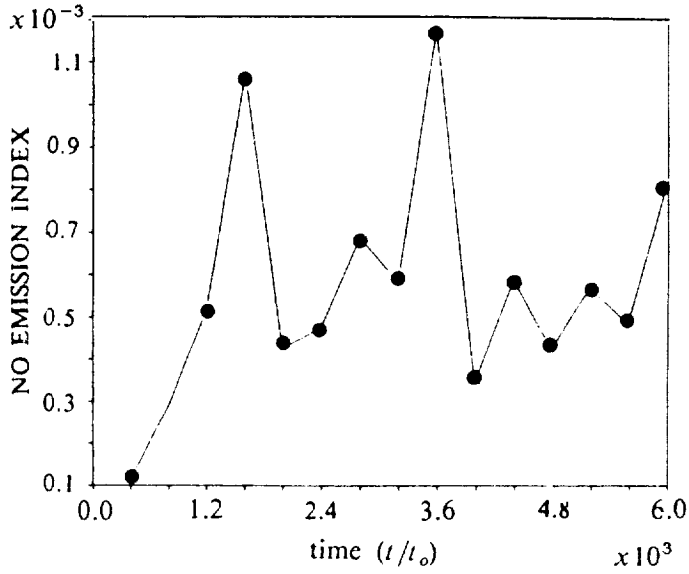

c. NO Emission Index for test case P-3 (u_{jet} = 48 m/s)

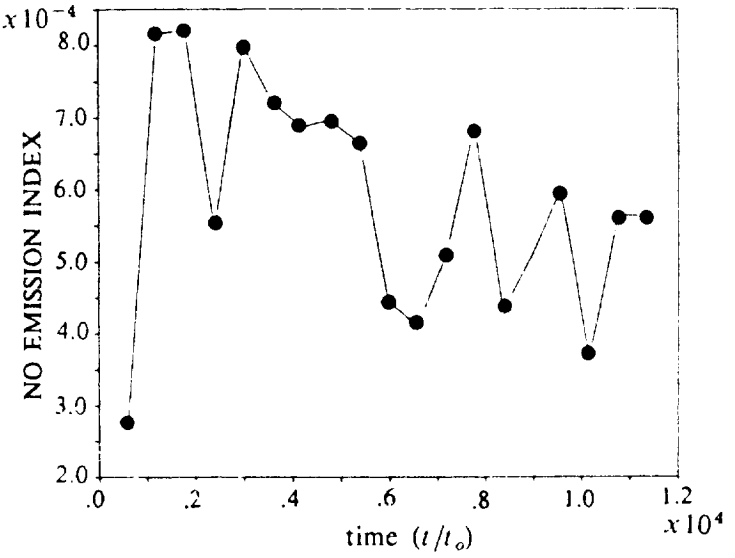

d. NO Emission Index for test case P-4 (u_{jet} = 72 m/s)

Figure 14. Evolution of the NO Emission Index (in *kg/kg of fuel*) as a function of time for various fuel jet speeds. Propane-air combustion for test cases P-1 through P-4.
Solid circles denote locations where NO Emission Index was recorded.

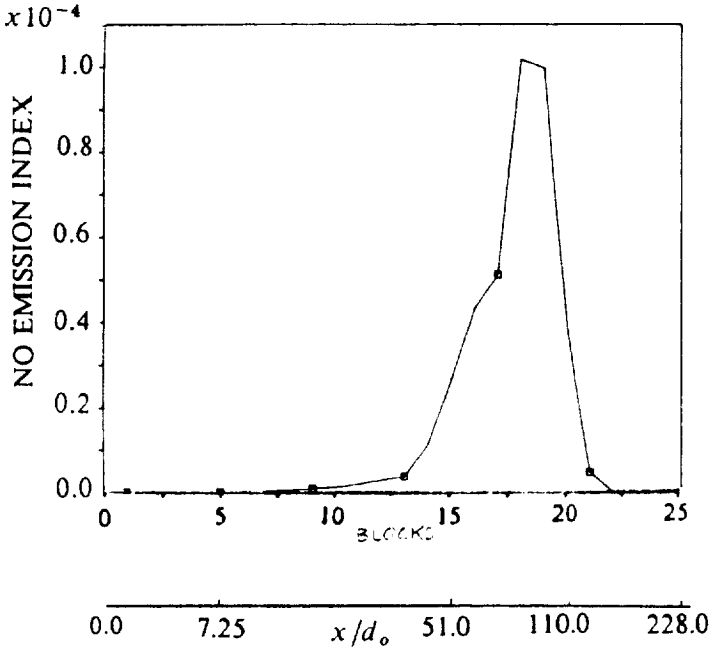

a. Test case P-1 (u_{jet} = 12 m/s)

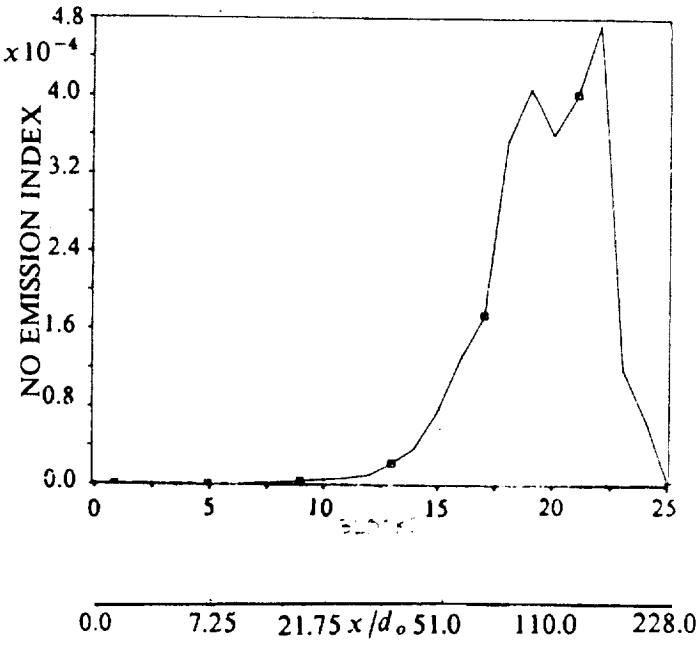

b. Test case P-2 (u_{jet} = 24 m/s)

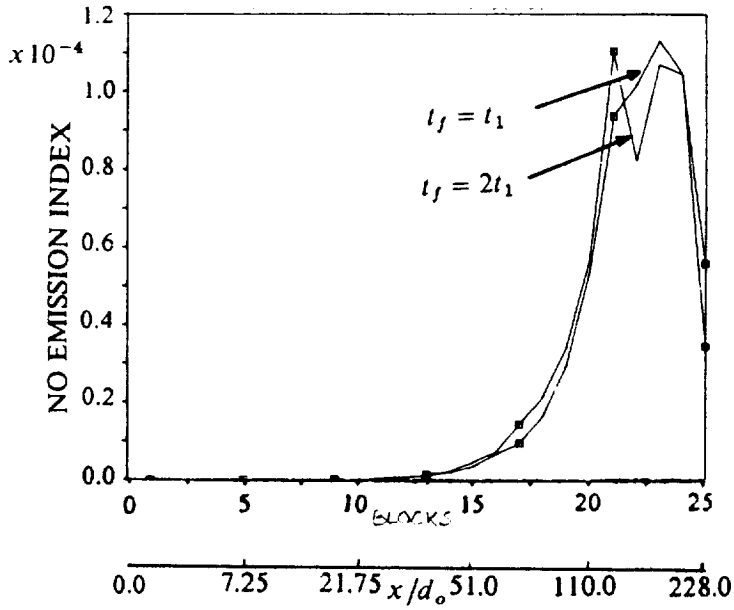

c. Test case P-3 (u_{jet} = 48 m/s)

Figure 15. Axial variation of nitric oxide production rate for various fuel jet speeds. Propane-air combustion cases P-1 to P-3.

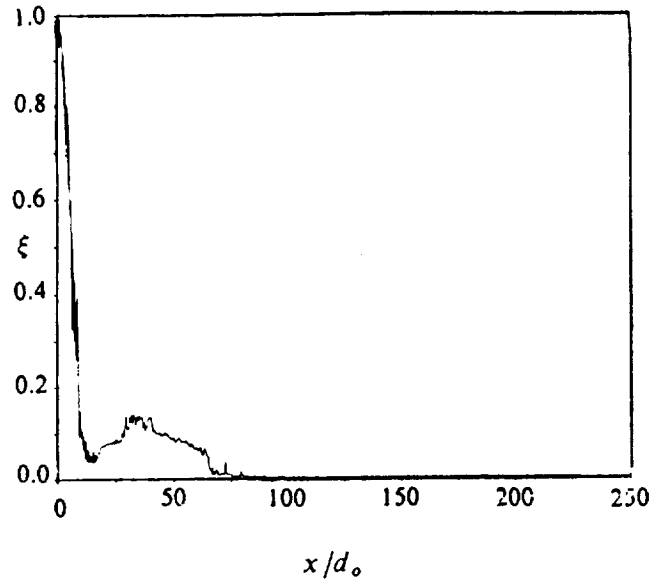

a. Mixture fraction (ξ)

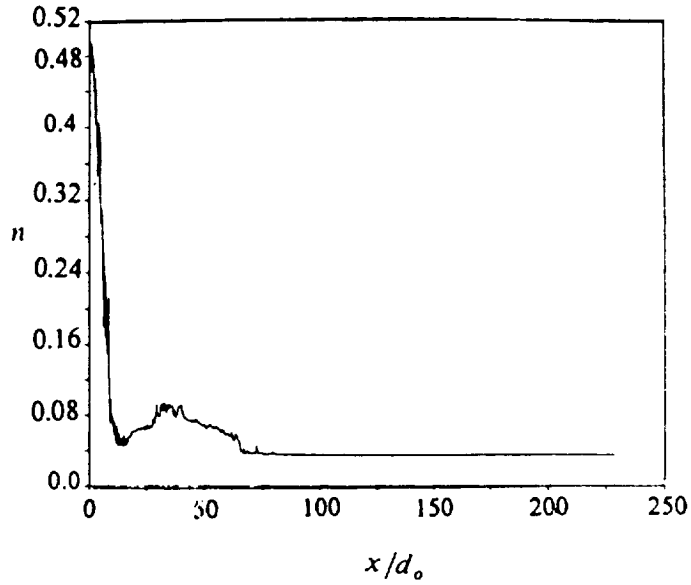

b. Progress variable (n) [*kmoles /kg*]

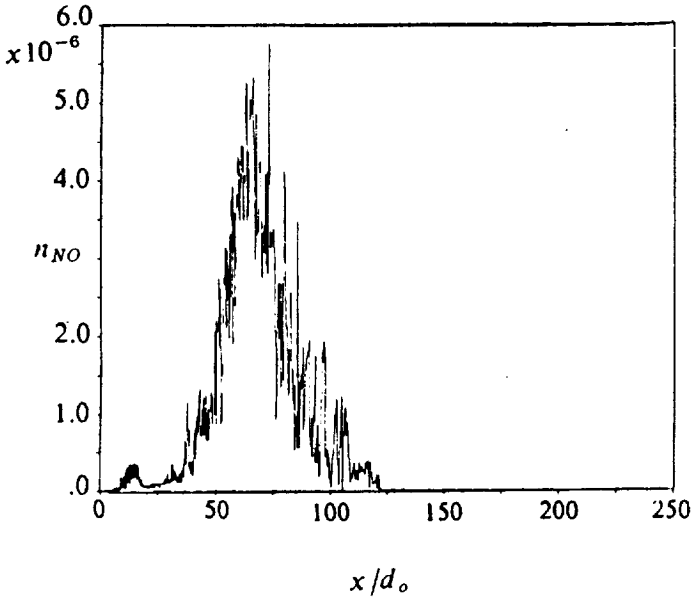

c. Nitric Oxide (n_{NO}) [*kmoles /kg*]

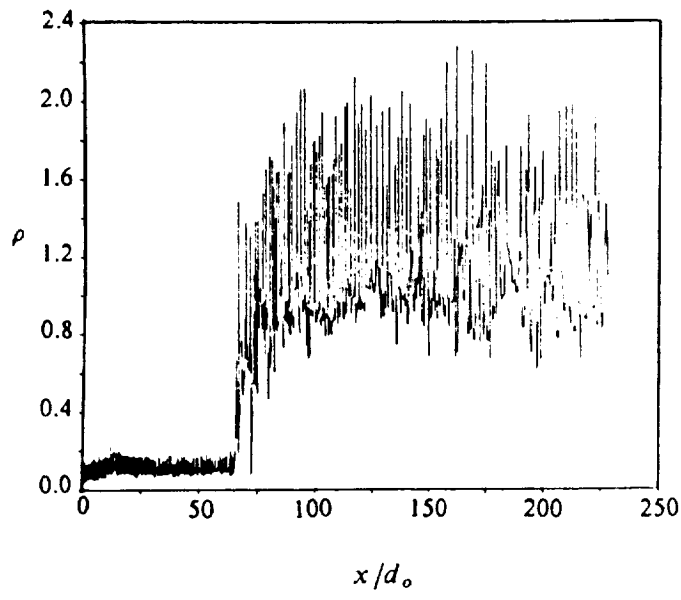

d. Density (ρ) [*kg /m*^{3}]

Figure 16. Axial variation of flow properties during hydrogen-air combustion. Test case H-2 (see Table III).

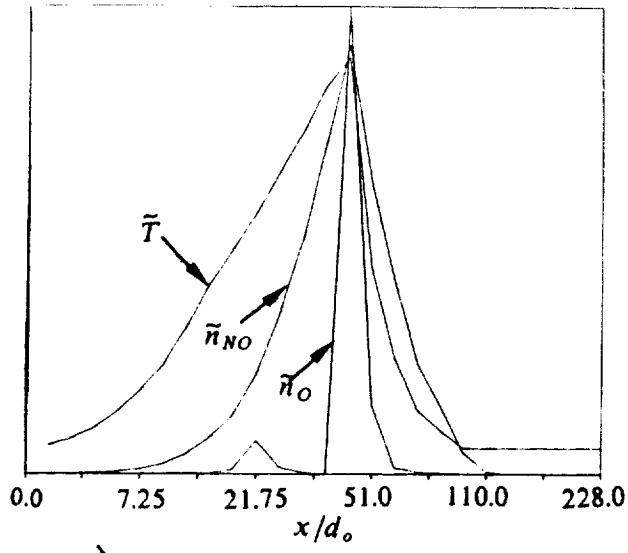

a. Nitric Oxide ($\tilde{n}_{NO}$), Oxygen atom ($\tilde{n}_O$) in [*kmoles /kg*] and Temperature ($\tilde{T}$) [K]

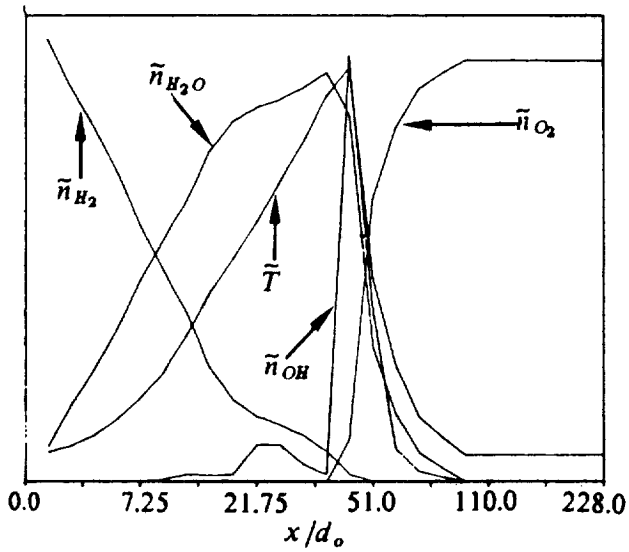

b. Water ($\tilde{n}_{H_2O}$), Hydrogen ($\tilde{n}_{H_2}$), Hydroxyl ($\tilde{n}_{OH}$), Oxygen ($\tilde{n}_{O_2}$) in [*kmoles /kg*] and Temperature ($\tilde{T}$) in [K]

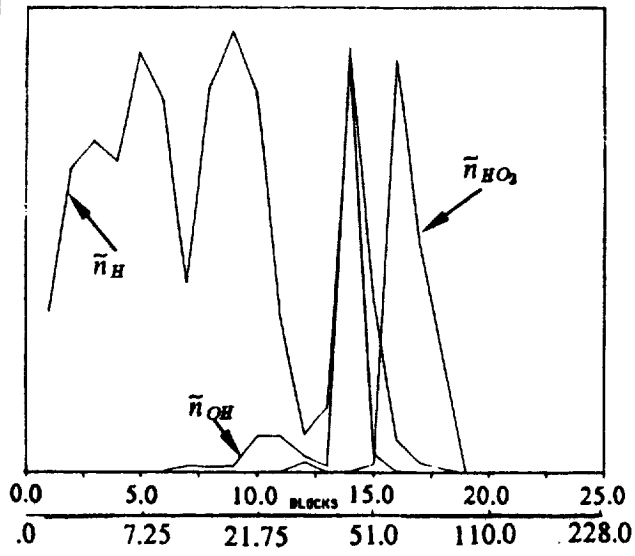

c. Hydrogen atom ($\tilde{n}_H$), Hydroxyl ($\tilde{n}_{OH}$), and Hydrogen dioxide ($\tilde{n}_{HO_2}$) in [*kmoles /kg*]

Figure 17. Axial variation of Favre-averaged species during Hydrogen-air combustion. Test case H-2 (see Table III).

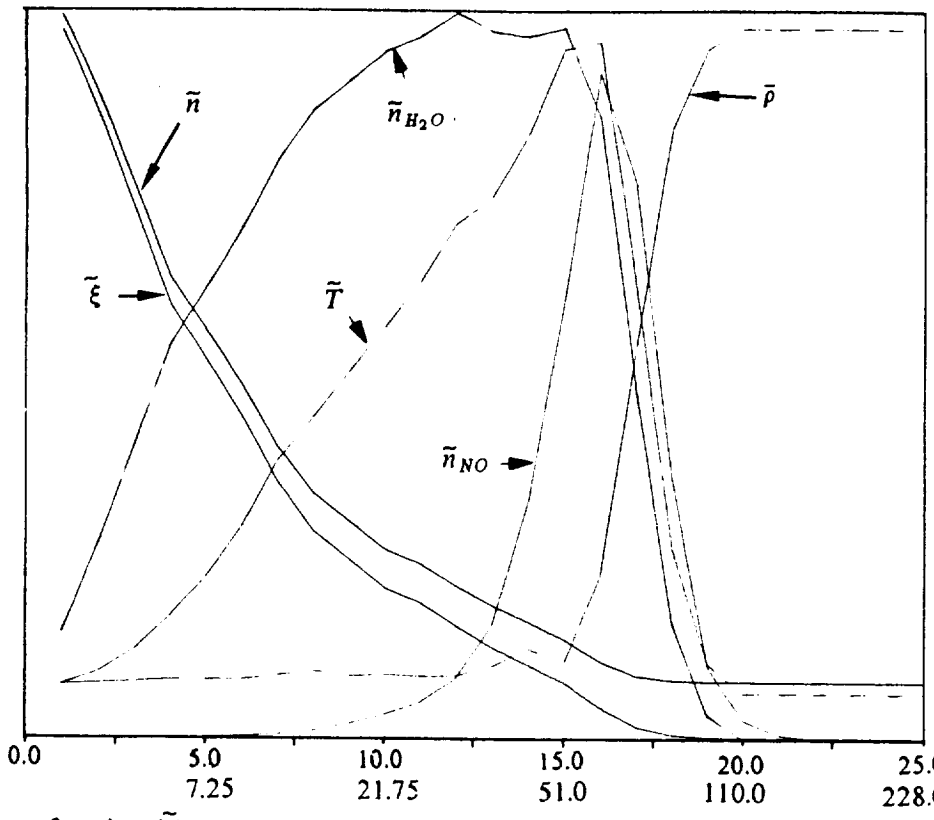

a. Mixture fraction ($\tilde{\xi}$), progress variable ($\tilde{n}$), Water ($\tilde{n}_{H_2O}$), Nitric Oxide ($\tilde{n}_{NO}$) in [*kmoles /kg*], Temperature ($\tilde{T}$) in [K] and density ($\bar{\rho}$) in [kg/m^3]

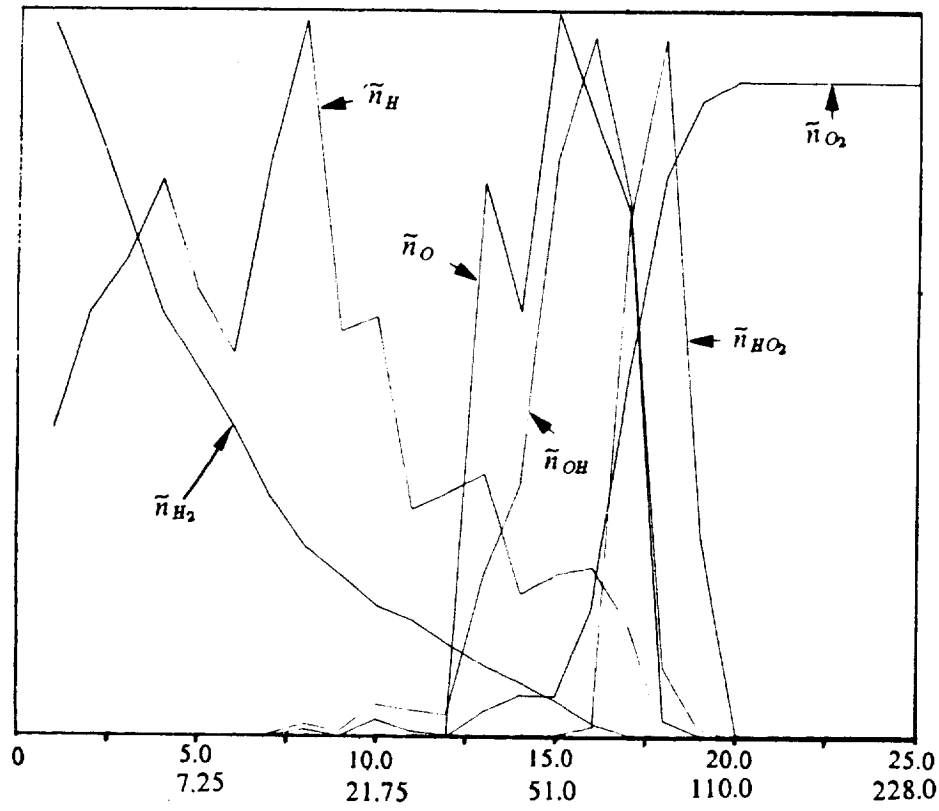

b. Hydrogen ($\tilde{n}_{H_2}$), Hydroxyl ($\tilde{n}_{OH}$), Oxygen ($\tilde{n}_{O_2}$), Hydrogen atom ($\tilde{n}_H$), Oxygen atom ($\tilde{n}_O$), and Hydrogen dioxide ($\tilde{n}_{HO_2}$) in [*kmoles /kg*]

Figure 18. Axial variation of Favre-averaged flow properties during Hydrogen-air combustion. Test case H-3 (see Table III).

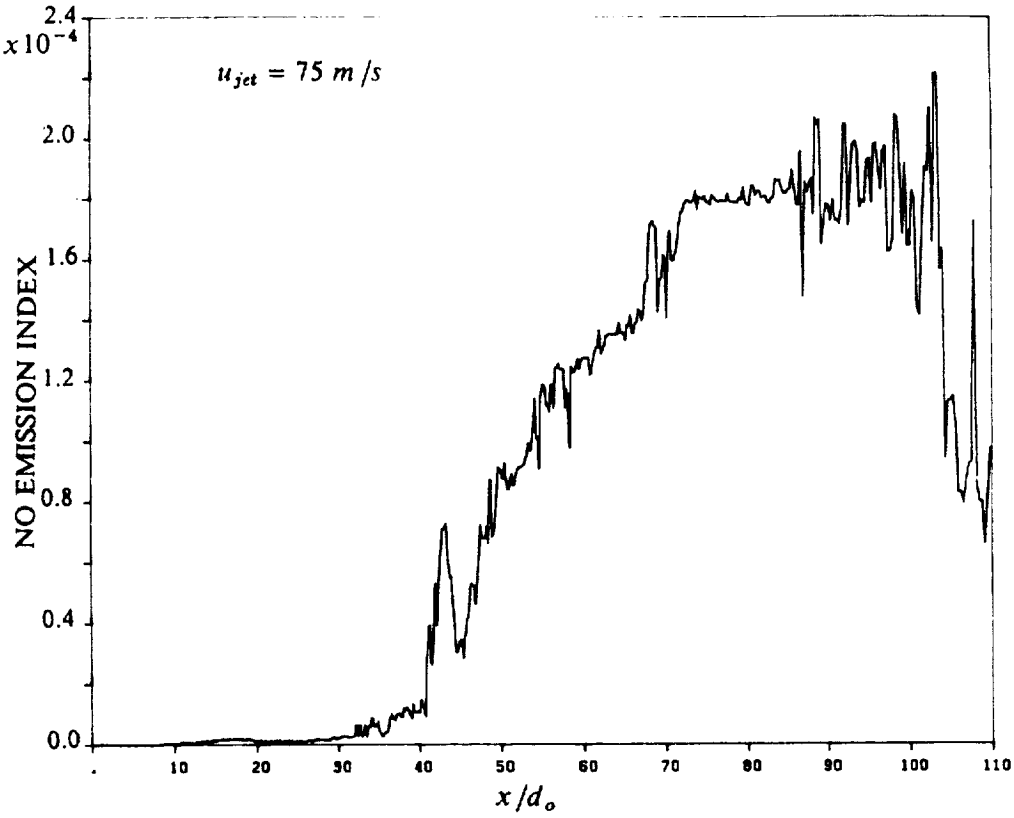

a. Test case H-1

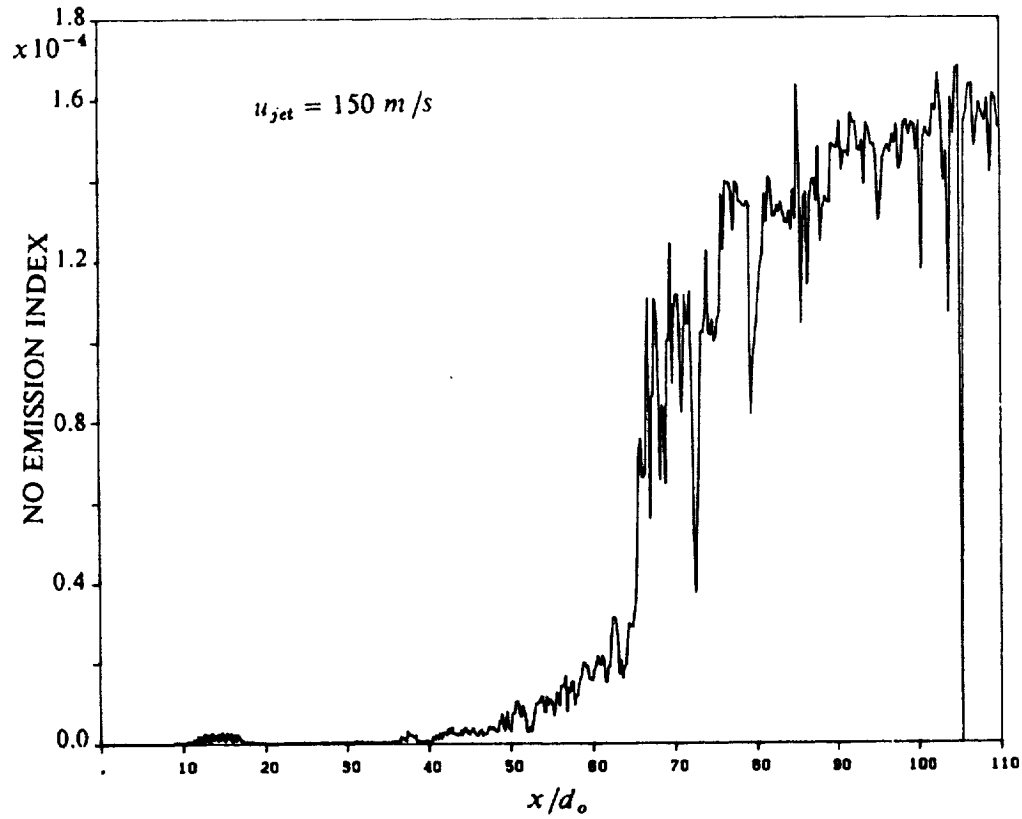

b. Test case H-2

Figure 19. Axial variation of the NO Emission Index (in *kg/kg of fuel*) for different fuel jet speeds.

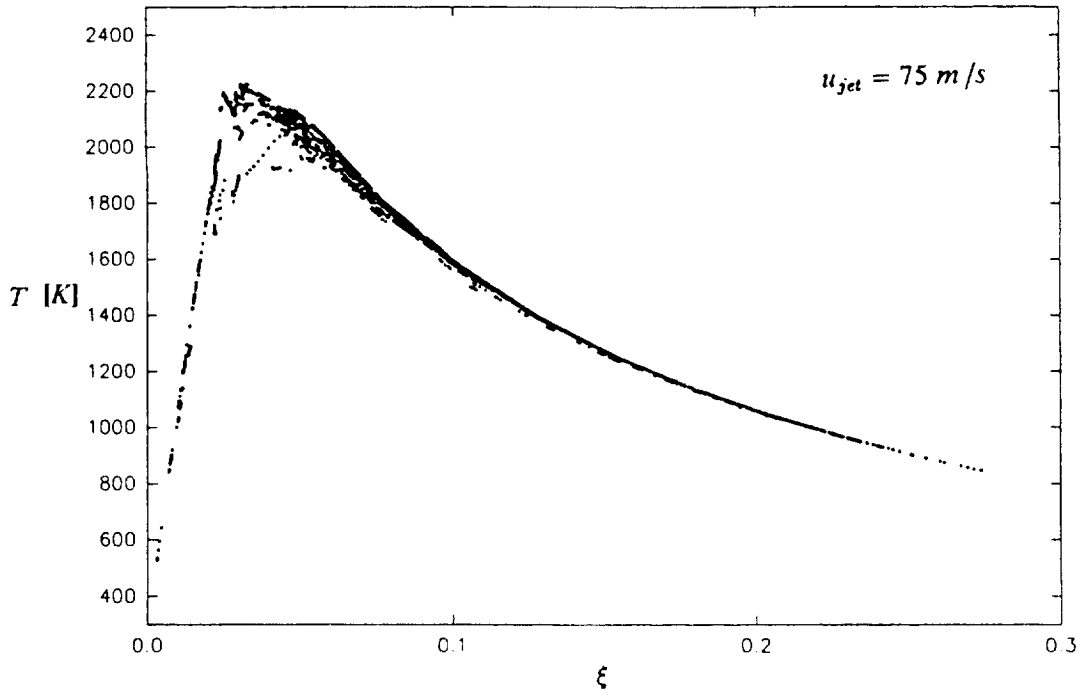

a. Test case H-1

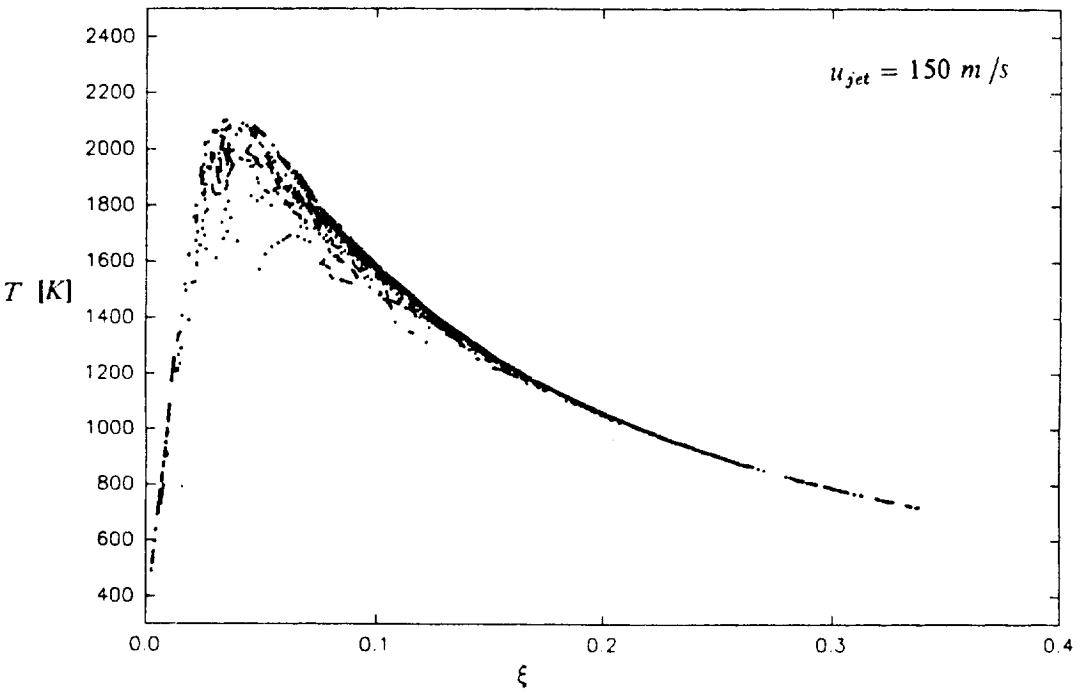

b. Test case H-2

Figure 20. Scatter plot of temperature as a function of mixture fraction for different fuel jet speeds at $x/d_0 = 30$. Hydrogen-air combustion (with pure hydrogen in the fuel jet)

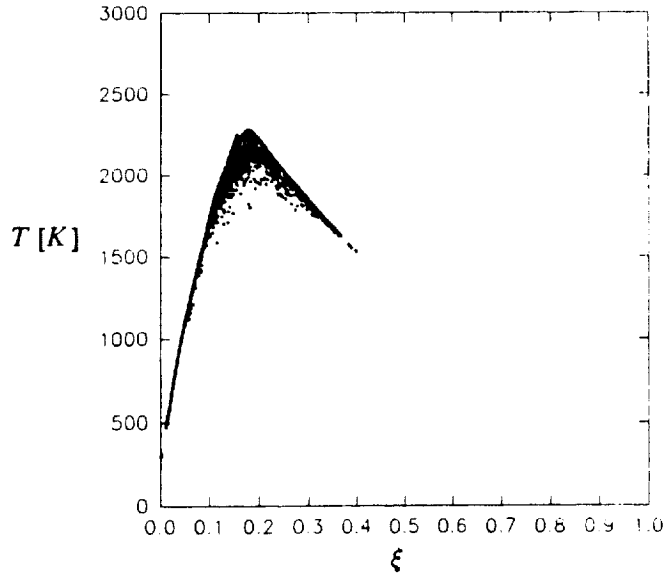

a. Test case H-3 (see Table III)

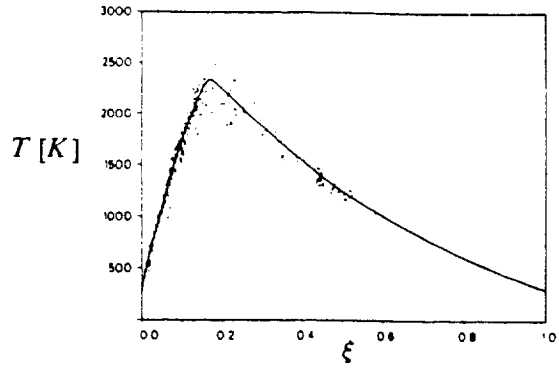

b. Experimental data (Magre and Dibble, 1988)

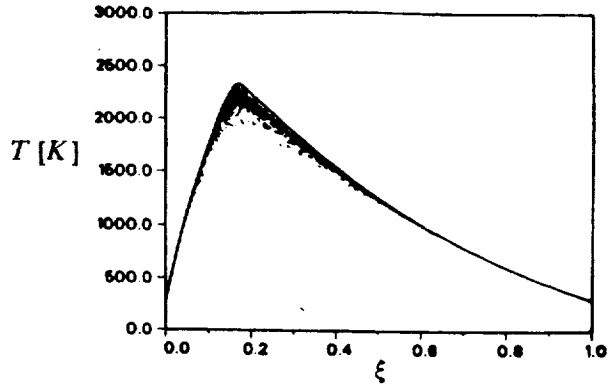

c. Pdf calculation (Chen and Kollmann, 1990)

Figure 21. Comparison of computed and experimental scatter plot of temperature as a function of mixture fraction. Hydrogen-air combustion (with 22%Argon + 78%Hydrogen in the fuel jet) ($u_{jet} = 75\ m/s$)

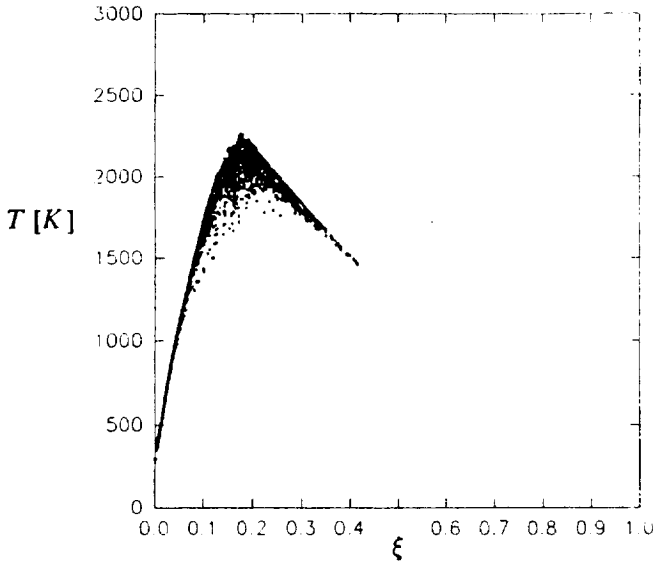

a. Test case H-4 (see Table III)

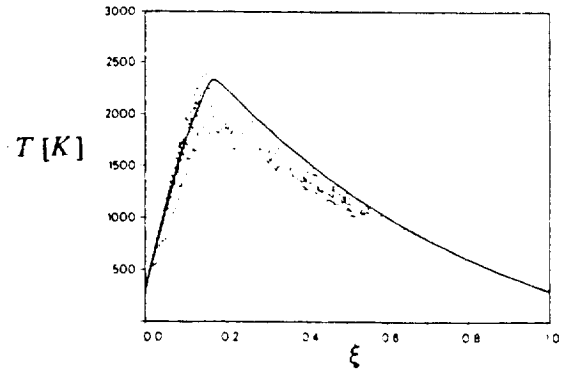

b. Experimental data (Magre and Dibble, 1988)

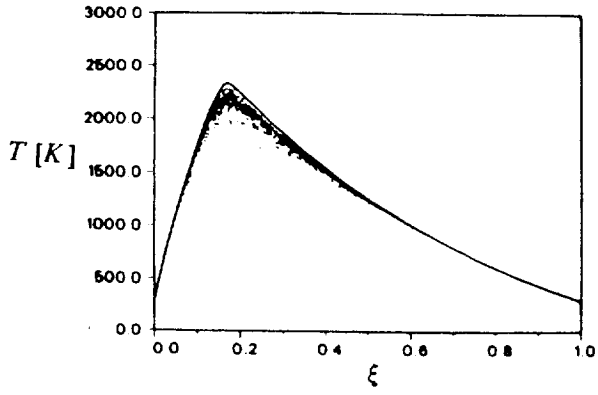

c. Pdf calculation (Chen and Kollmann, 1990)

Figure 22. Comparison of computed and experimental scatter plot of temperature as a function of mixture fraction. Hydrogen-air combustion (with 22%Argon + 78%Hydrogen in the fuel jet) (u_{jet} = 150 m/s)

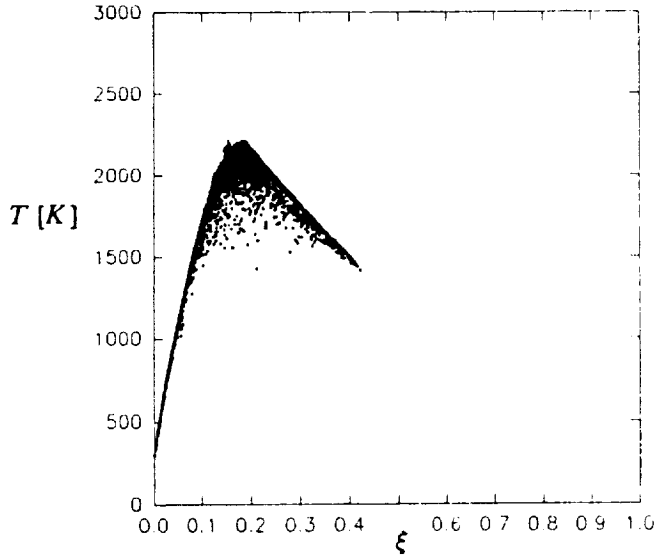

a. Test case H-5 (see Table III)

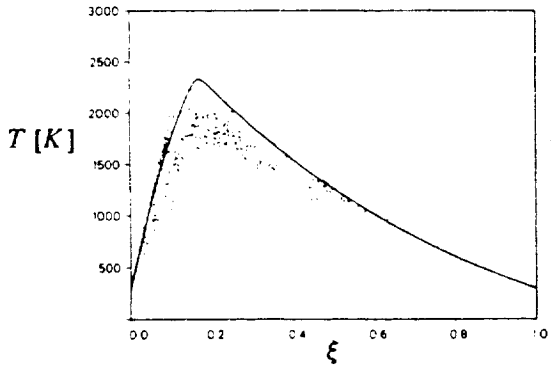

b. Experimental data (Magre and Dibble, 1988)

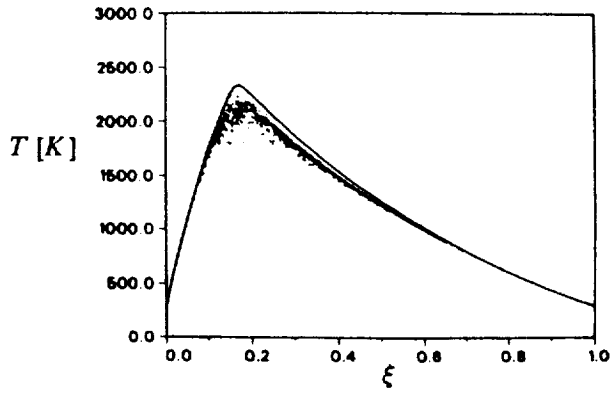

c. Pdf calculation (Chen and Kollmann, 1990)

Figure 23. Comparison of computed and experimental scatter plot of temperature as a function of mixture fraction. Hydrogen-air combustion (with 22%Argon + 78%Hydrogen in the fuel jet) (u_{jet} = 225 m/s)

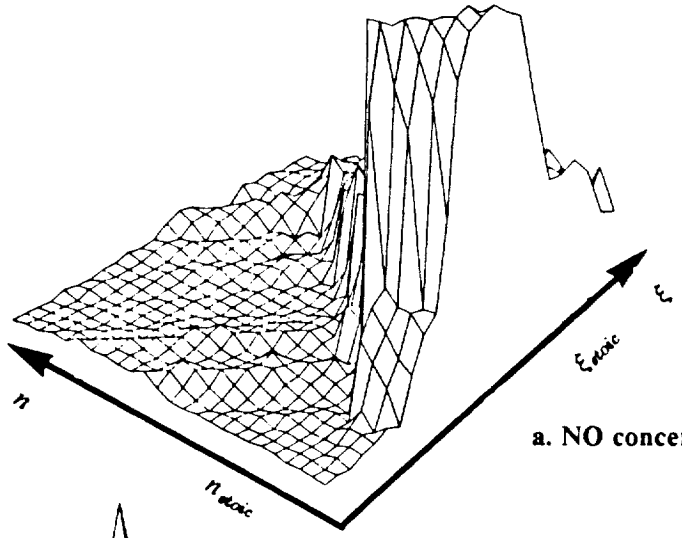

a. NO concentration in the $\xi - n$ space. Test case H-4

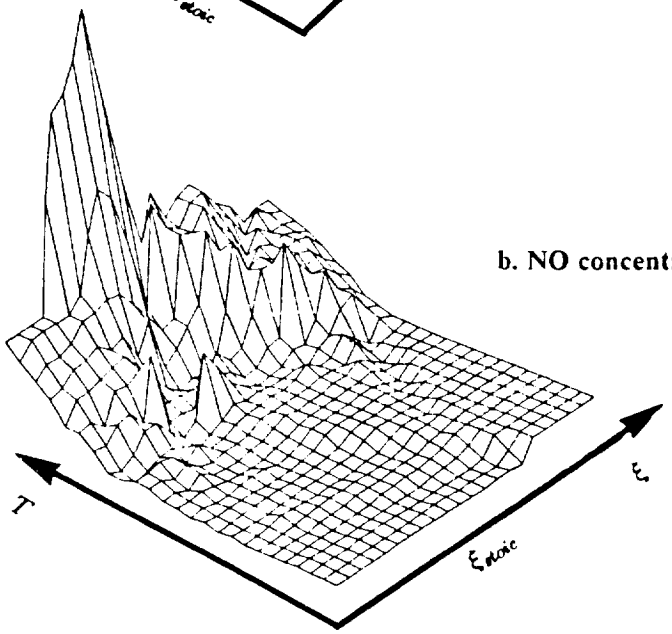

b. NO concentration in the $T - \xi$ space. Test case H-4

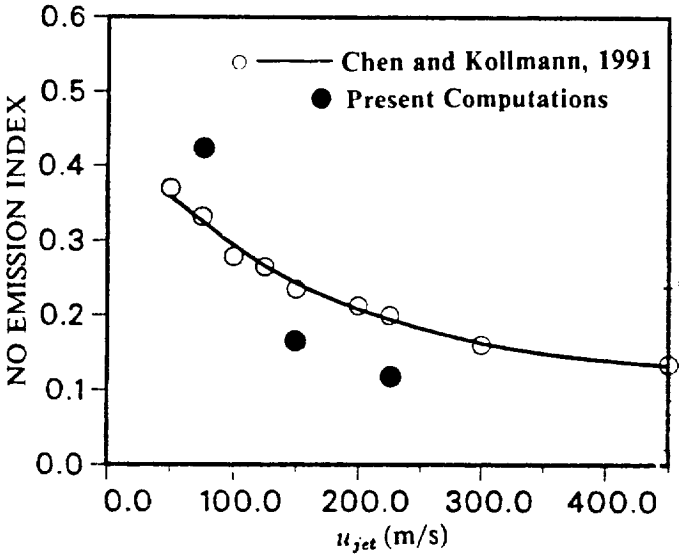

c. NO Emission Index (gm / kg of fuel) as a function of jet speed

Figure 24. The NO Emission dependence on temperature, mixture fraction, progress variable and fuel jet speed. 22%Argon+78%Hydrogen combustion case.

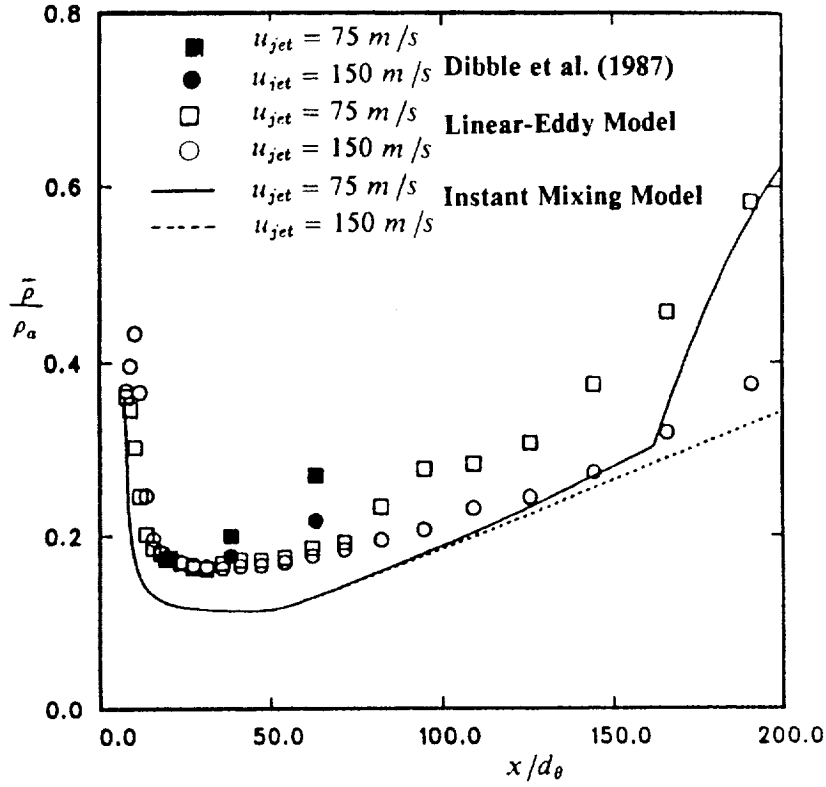

Figure 25. Axial variation of time-averaged density. 22%Argon+78%Hydrogen-air combustion case modeled using equilibrium assumptions (Kerstein, 1991a).

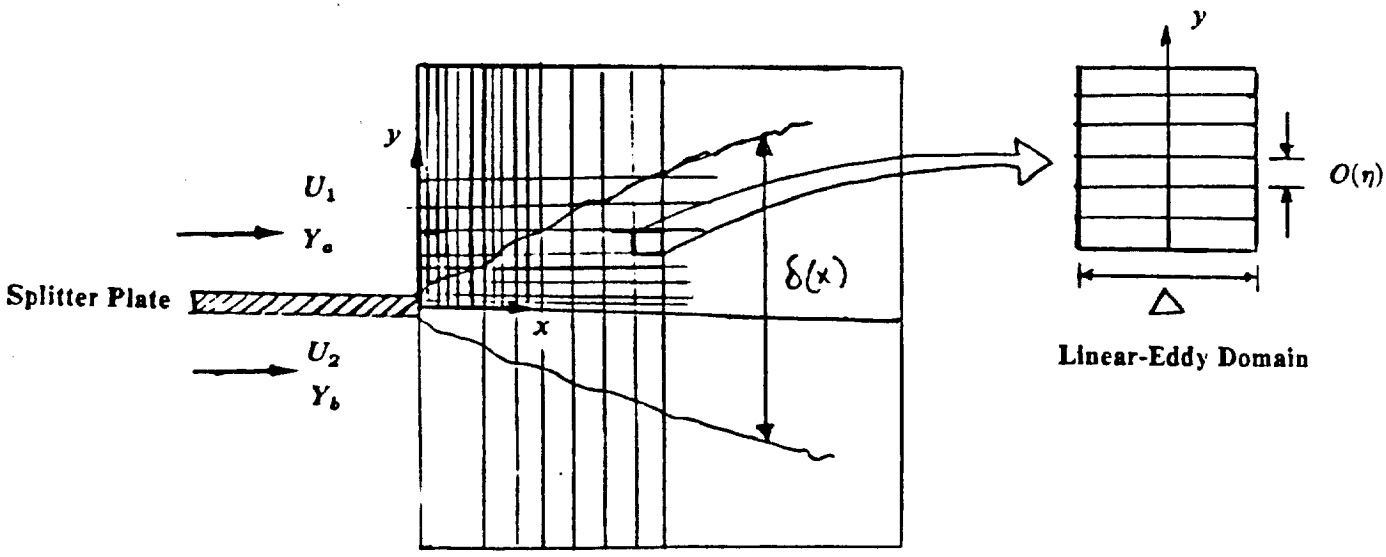

Figure 26. Schematic of a spatially developing shear layer and the implementation of the linear-eddy mixing model within the large-scale grid.

REPORT DOCUMENTATION PAGE

Form Approved
OMB No. 0704-0188

1. AGENCY USE ONLY (Leave blank)	2. REPORT DATE	3. REPORT TYPE AND DATES COVERED
	April 1992	Final Contractor Report

4. TITLE AND SUBTITLE

A New Unsteady Mixing Model to Predict NO_x Production During Rapid Mixing in a Dual-Stage Combustor

5. FUNDING NUMBERS

WU–324–02–00
C–NAS3–26242

6. AUTHOR(S)

Suresh Menon

7. PERFORMING ORGANIZATION NAME(S) AND ADDRESS(ES)

QUEST Integrated, Inc.
21414–68th Avenue South
Kent, Washington 98032

8. PERFORMING ORGANIZATION REPORT NUMBER

None

9. SPONSORING/MONITORING AGENCY NAMES(S) AND ADDRESS(ES)

National Aeronautics and Space Administration
Lewis Research Center
Cleveland, Ohio 44135–3191

10. SPONSORING/MONITORING AGENCY REPORT NUMBER

NASA CR–189155
QUEST Technical Report 534

11. SUPPLEMENTARY NOTES

Project Manager, James D. Holdeman, Internal Fluid Mechanics Division, NASA Lewis Research Center, (216) 433–5846.

12a. DISTRIBUTION/AVAILABILITY STATEMENT

Unclassified - Unlimited
Subject Category 07

12b. DISTRIBUTION CODE

13. ABSTRACT ***(Maximum 200 words)***

An advanced gas turbine engine to power supersonic transport aircraft is currently under study. In addition to high combustion efficiency requirements, environmental concerns have placed stringent restrictions on the pollutant emissions from these engines. A combustor design with the potential for minimizing pollutants such as NO_x emissions is undergoing experimental evaluation. A major technical issue in the design of this combustor is how to rapidly mix the hot, fuel-rich primary zone product with the secondary diluent air to obtain a fuel-lean mixture for combustion in the secondary stage. Numerical predictions using steady-state methods cannot account for the unsteady phenomena in the mixing region. Therefore, to evaluate the effect of unsteady mixing and combustion processes, a novel unsteady mixing model is demonstrated here. This model has been used to study multispecies mixing as well as propane-air and hydrogen-air jet nonpremixed flames, and has been used to predict NO_x production in the mixing region. Comparison with available experimental data show good agreement thereby providing validation of the mixing model. With this demonstration, this mixing model is ready to be implemented in conjunction with steady-state prediction methods and provide an improved engineering design analysis tool.

14. SUBJECT TERMS

NO_x production; Rapid mixing; Linear eddy; Combustion; Turbulent mixing; Finite-rate kinetics; Entrainment; Molecular diffusion

15. NUMBER OF PAGES
58

16. PRICE CODE
A04

17. SECURITY CLASSIFICATION OF REPORT	18. SECURITY CLASSIFICATION OF THIS PAGE	19. SECURITY CLASSIFICATION OF ABSTRACT	20. LIMITATION OF ABSTRACT
Unclassified	Unclassified	Unclassified	